

# Young and embedded clusters in Cygnus-X: evidence for building up the IMF?

F. F. S. Maia<sup>1,2,3\*</sup>, E. Moraux<sup>1,2</sup> and I. Joncour<sup>1,2</sup>

<sup>1</sup>Univ. Grenoble Alpes, IPAG, F-38000 Grenoble, France

<sup>2</sup>CNRS, IPAG, F-38000 Grenoble, France

<sup>3</sup>CAPES Foundation, Ministry of Education of Brazil, Brasília - DF 70040-020, Brazil

Accepted for publication in MNRAS

## ABSTRACT

We provide a new view on the Cygnus-X north complex by accessing for the first time the low mass content of young stellar populations in the region. CFHT/WIRCam camera was used to perform a deep near-IR survey of this complex, sampling stellar masses down to  $\sim 0.1 M_{\odot}$ . Several analysis tools, including a extinction treatment developed in this work, were employed to identify and uniformly characterise a dozen unstudied young star clusters in the area. Investigation of their mass distributions in low-mass domain revealed a relatively uniform log-normal IMF with a characteristic mass of  $0.32 \pm 0.08 M_{\odot}$  and mass dispersion of  $0.40 \pm 0.06$ . In the high mass regime, their derived slopes showed that while the youngest clusters (age  $< 4$  Myr) presented slightly shallower values with respect to the Salpeter's, our older clusters ( $4 \text{ Myr} < \text{age} < 18 \text{ Myr}$ ) showed IMF compliant values and a slightly denser stellar population. Although possibly evidencing a deviation from an 'universal' IMF, these results also supports a scenario where these gas dominated young clusters gradually 'build up' their IMF by accreting low-mass stars formed in their vicinity during their first  $\sim 3$  Myr, before the gas expulsion phase, emerging at the age of  $\sim 4$  Myr with a fully fledged IMF. Finally, the derived distances to these clusters confirmed the existence of at least 3 different star forming regions throughout Cygnus-X north complex, at distances of 500-900 pc, 1.4-1.7 kpc and 3.0 kpc, and revealed evidence of a possible interaction between some of these stellar populations and the Cygnus-OB2 association.

**Key words:** open clusters and associations: Cygnus-X – infrared: stars – stars: pre-main-sequence – stars: low mass – stars: luminosity function, mass function

## 1 INTRODUCTION

The Cygnus X area is one of the richest star forming regions (SFR) known in the Galaxy. It presents an extended structure to which are associated numerous optical, infrared and radio objects. Early studies divided this region into 9 OB associations (Humphreys 1978) housing over a thousand OB stars and tens of compact HII regions and stellar nurseries. Inside these large associations several concentrations have been recognised as young stellar clusters or embedded agglomerates (Comerón & Torra 2001; Dutra & Bica 2001).

However, observational efforts to study this region have been hampered by heavy absorption with complex patterns caused by a foreground molecular cloud structure known as the Great Cygnus Rift, that also appears to harbour star formation (Knödlseeder 2000). Moreover, when looking towards Cygnus the local spiral arm is seen tangentially, so that structures at different distances superpose

in the line of sight, causing confusion as to the real spatial structure and content of these associations.

For example, although Cygnus-X is actually divided into two large molecular cloud complexes (Cygnus-X north and Cygnus-X south) separated by a large clearing hosting the Cygnus OB2 association, it is still not clear whether the north and south cloud complexes are related to each other or to the Cygnus OB2 association projected between them (Kryukova et al. 2014). Recent investigation on the OB stars (Comerón et al. 2008; Wright, Drew, & Mohr-Smith 2015) indicates that star formation has been ongoing for the last  $\sim 10$  Myr in the region, taking place early in its southern region and then later in Cygnus OB2 and the northern complex, thus generating a mixture of different aged populations in the field. However it is not understood if these events happened in a triggered manner since the distance to these regions are not well constrained.

In this matter, radio CO imaging of the gaseous content by Schneider et al. (2006) indicated that all the structures in the Cygnus-X region were interconnected, probably at the same distance of Cygnus OB2. Such findings were somewhat supported by

\* E-mail: francisco.maia@obs.ujf-grenoble.fr

maser parallaxes done by Rygl et al. (2012, hereafter R12) on 5 discrete sources across the northern complex, finding a mean distance of 1.4 kpc. However, higher resolution CO mapping by Gottschalk et al. (2012, hereafter G12) uncovered a much more complex gas structure towards Cygnus-X north, detecting three distinct layers of CO emission related to (i) the Great Cygnus Rift at 500-800 pc, (ii) W75 and DR17 at 1.0-1.8 kpc and (iii) DR21 at 1.5-2.5 kpc.

In this context, the many young star clusters in this region had been largely neglected. These objects are excellent probes from which a range of physical parameters can be determined. Recent work on the characterisation of Cygnus stellar clusters has largely used infrared data from the Two Micron All Sky Survey (2MASS) (Bica, Dutra, & Barbuy 2003; Le Duigou & Knödseder 2002, hereafter LK02), mostly due to its prompt availability and ability to probe considerably deeper than optical surveys. It is clear however that deeper photometry is needed to properly investigate this region. The moderate distance ( $m-M \approx 11$ ) and high reddening ( $A_K \approx 3.0$ ) towards this region can make the 2MASS sample highly incomplete for stars fainter than A0 spectral type ( $\sim 5 M_\odot$ ).

The most comprehensive study of the young clusters in this region has been performed by LK02, who detected 11 previously unknown stellar clusters in the area and characterised the morphology and the stellar content of total sample of 22 targets. However, due to the limitations of the data, the authors did not determine ages nor distances for many of their targets adopting instead the mean values for the Cygnus population, thus precluding a global analysis of the region based on the cluster parameters.

To address this issue, we have acquired deep near-infrared (NIR) images of a large extent of the Cygnus-X north complex ( $\sim 1^\circ \times 1^\circ$ ) including a dozen of catalogued clusters and HII regions and reaching about 4 magnitudes deeper than previous studies, often sampling stellar masses down to  $0.1 M_\odot$ . We have developed a method to constrain most probable age and distance intervals for a given stellar population using the statistical distributions of stellar extinction, derived via (stellar) evolutionary models. Age, distance, extinction, structural parameters and mass distribution were determined for each catalogued object and used to get an overall view of the Cygnus-X north.

This paper is organised as follows. In Sect. 2 we describe the observations and processing of our data as well as the photometry and calibration. Sect. 3 describes our cluster sample and Sect. 4 the methodology adopted for investigating it. Our results and conclusions are drawn in Sect. 5 and 6 respectively.

## 2 DATA HANDLING

### 2.1 Acquisition and processing

The Wide-Field Infrared Camera (WIRCam) at the Canadian-France-Hawaii Telescope (CFHT) was employed to observe five fields inside a Cygnus-X cloud complex located about 1.5 deg. to the northeast of the centre of the Cygnus OB2 association. An IRIS (Miville-Deschênes & Lagache 2005)  $100\mu\text{m}$  dust emission contour map of this region is shown in Fig. 1 depicting the position of the observed WIRCam fields. Catalogued stellar clusters and HII regions in the field (see Sect. 3) are also shown.

Observations were carried out under photometric conditions in six nights between 04/09/12 and 29/10/12, yielding seeing values between  $0.6''$  and  $0.9''$ . The total integration time in each filter was 960s in  $J$ , 1200s in  $H$  and 480s in  $K_s$ , designed as to provide good quality photometry ( $S/N \approx 25$ ) down to the following magnitude

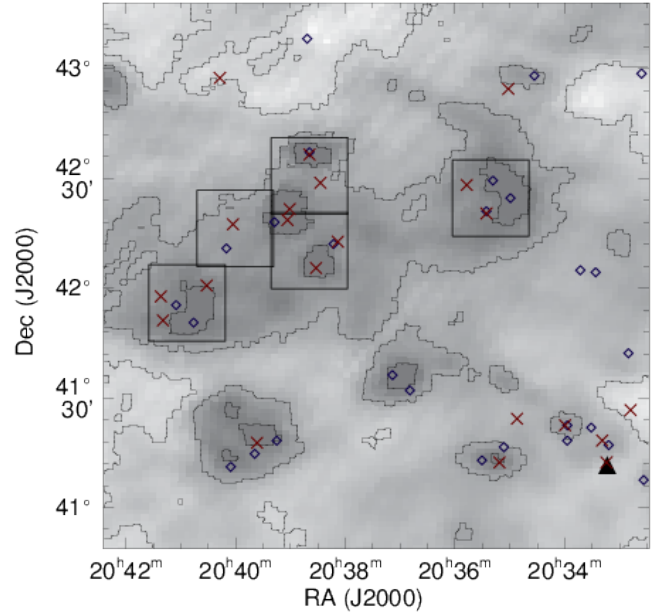


**Figure 1.** IRIS  $100\mu\text{m}$  dust emission contour map of the region of interest, located  $\sim 1.5$  deg. northeast of the Cygnus OB2 association centre (black triangle). The observed WIRCam fields (squares), known clusters (crosses) and HII regions (diamonds) in the region are also shown. Contour levels are at 150, 300, 750 and 2000 MJy/sr.

limits:  $J \approx 20.0$ ,  $H \approx 19.5$  and  $K_s \approx 18.5$ . These limits were chosen to sample stars in the sub-solar mass regime, considering the mean extinction and distance of this cloud complex (LK02). As usual for near-infrared imaging, these integration times were fragmented into several short exposures composing a dither pattern with more than 20 positions in each field.

Data detrending was carried out at CFHT using the WIRCam pipeline, 'Tiwi'. Post-processing of the data included recalculation of the astrometric solution against the Two Micron All Sky Survey (2MASS) catalogue (Skrutskie et al. 2006) with the SCAMP software (Bertin 2006), and resampling and co-addition of  $\sim 500$  individual frames into three master mosaics (one in each filter) with the SWARP software (Bertin et al. 2002). The astrometric recalibration was very precise, with RMS residuals about  $\sim 0.05''$  internally and  $\sim 0.12''$  in relation to 2MASS, well below the WIRCam pixel size ( $0.3''$ ). Furthermore, a comparative inspection of the images have shown no considerable ( $< 10\%$ ) degradation of the point-spread function (PSF) in the resulting mosaics when compared to the individual frames. Finally, the derived map of the PSF FWHM in the resulting mosaics (see next section) showed a smooth solution with values ranging from  $0.6''$  to  $1.0''$ , consistent with the reported seeing values on the individual frames.

### 2.2 Photometry

Source extraction and PSF modelling was carried out in the master mosaics using SExtractor and PSFEx softwares (Bertin 2011) interactively. Initially, source detection was done at the  $2-\sigma$  level in the deeper mosaic ( $K_s$ ) without employing any image filtering, as to maximize the recovery of fainter objects, particularly near bright objects. This initial catalogue was filtered out of artefacts, spurious detections and extended sources by using morphological parameters derived from the sources isophotal profiles (e.g. ellipticity,

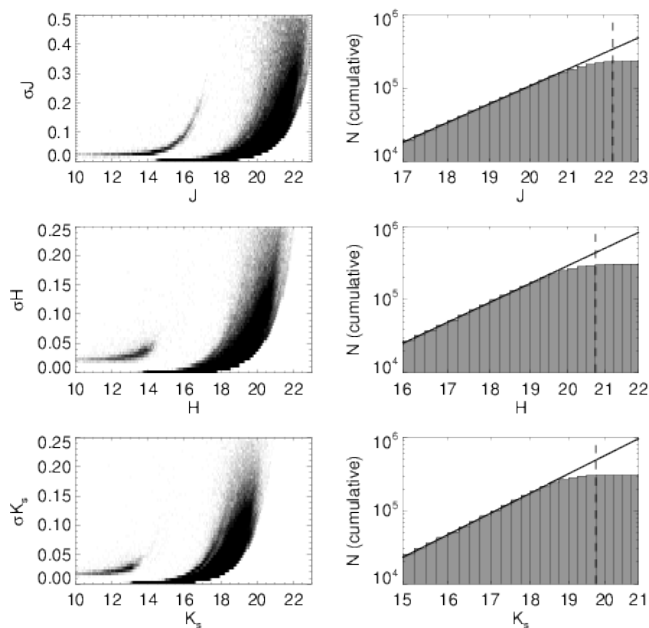


**Figure 2.** Derived photometric uncertainties (left panels) and cumulative source counts (right panels) as function of the derived PSF magnitude in filters  $J$  (upper panels),  $H$  (middle panels) and  $K_s$  (bottom panels). The brighter uncertainty regime in the left panels are due to recovered 2MASS sources (see text). In the right panels, the 50% completeness level (vertical dashed lines) were estimated from the extrapolated stellar numbers (solid lines).

half-light radius) and local PSF parameters (e.g. FWHM, reduced  $\chi^2$ ) to generate a filtered catalogue containing about  $3 \times 10^5$  stars. Finally, Kron-like elliptical apertures and PSF fitting were carried out independently in each mosaic ( $J$ ,  $H$  and  $K_s$ ) to derive fluxes and magnitudes for all sources in the filtered catalogue.

The left panels of Fig. 2 shows the magnitude uncertainties derived from the PSF photometry in each filter. From these values we found that the magnitude limits reached at a  $S/N \sim 25$  ( $\sigma=0.04$ ) were  $J \sim 20.5$ ,  $H \sim 20.0$ ,  $K_s \sim 19.0$ . The right panels of Fig. 2 show the cumulative source counts as a function of magnitude. In each diagram, a linear relation was fit to the brighter bins of the distribution allowing us to extrapolate the expected source counts for the fainter bins and estimate the source incompleteness as a function of the magnitude. Therefore, we have derived the 50% completeness level at:  $J_{50}=22.25$ ,  $H_{50}=20.75$ ,  $K_{s,50}=19.75$  and the 95% completeness level at:  $J_{95}=20.75$ ,  $H_{95}=19.50$ ,  $K_{s,95}=18.50$ .

While these derived completeness limits should be appropriate for most of the overall field population, higher than average incompleteness is expected near the clusters centre, due to crowding effects. Therefore, a more rigorous completeness estimate was conducted in a large region around each cluster by adding artificial stars in a regular grid with a  $\sim 6''$  spacing, corresponding roughly to the size of the derived PSF. Local completeness was then estimated by redoing the photometry and calculating the artificial stars recovery fraction inside a  $\sim 30''$  kernel across each cluster region. This process was repeated several times in each filter, covering a wide range of magnitudes with 0.5 magnitude steps. Fig. 3 shows the derived completeness map around the cluster LK12 using artificial stars with  $K_{s,95}=18.50$ , corresponding to the 95% completeness level determined from stellar counts. It can be seen that, even if completeness level averages to  $\sim 86\%$  throughout this cluster re-

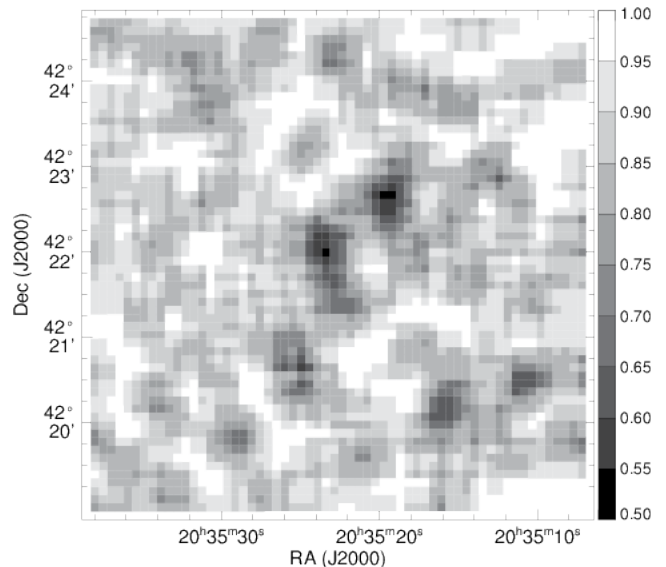


**Figure 3.** Completeness map derived for the cluster LK12, using artificial stars with  $K_s=18.5$ . Although the average completeness value throughout this map was found to be  $\sim 86\%$ , the densest parts of the cluster present local completeness values (represented by the colourbar) as low as 50%. Resolution of the map is  $\sim 30''$ .

gion, it can reach values as low as 50% in the more crowded regions near its centre.

The average completeness values calculated in those maps as function of magnitude is shown on the left panel of Fig. 4, for cluster LK12. It can be seen that completeness decreases from nearly 100% at bright magnitudes to  $\sim 86\%$  at  $K_{s,95}=18.50$ ,  $H_{95}=19.50$  and  $J_{95}=20.75$ . This implies that, although a small correction is still necessary to equalise the completeness levels as derived from stellar counts and artificial star simulations, they appear to be uniformly correlated across all bands. The right panel shows the total completeness as function of the distance to cluster centre, obtained by integrating the completeness maps in the  $K_s$ -band across the entire magnitude range tested, down to the  $K_{s,95}$  limit. As it can be seen, it is remarkable that, although completeness is lower towards the centre of LK12 it raises quickly to about 95% in the outer regions of the cluster, effectively matching the overall field completeness value found by star counts.

### 2.3 Calibration

Although WIRCam broad-band filters  $J$ ,  $H$  and  $K_s$  have response curves similar to the 2MASS filters, enough differences exists to justify a colour calibration between the two filter sets. Compared to the equivalent 2MASS filters, the WIRCam ones present a central wavelength that is slightly redder in the  $J$  filter and slightly bluer in the  $H$  and  $K_s$ , while also presenting significantly larger bandpasses in the  $H$  and  $K_s$  filters.

WIRCam observations usually presents a  $\sim 3$  magnitude overlap between its saturation limit and 2MASS completeness level thus allowing for a generous sample of common stars to derive a photometric calibration between the two datasets. In our dataset near 12000 common sources were found using a correlation radius threshold of  $0.8''$  between the datasets, derived from a nearest neighbour analysis of 2MASS sources relative to our catalogued sources, shown in Fig. 5. The adopted correlation distance

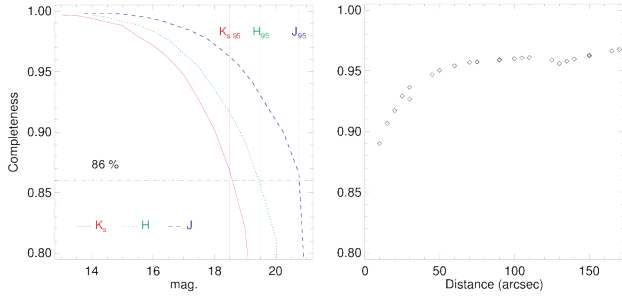


**Figure 4.** *Left:* Average completeness around LK12 as function of magnitude, derived from artificial star simulations in the  $J$ ,  $H$  and  $K_s$  bands (dashed, dotted and solid lines, respectively). The 95% completeness derived from stellar counts in each filter (vertical lines) corresponds approximately to a 86% level (horizontal line), as derived from artificial stars simulations. *Right:* Integrated completeness across all magnitudes fainter than  $K_{s,95}=18.50$ , as a function of the distance from LK12 centre. Although completeness is lower at the centre of the cluster, it raises in towards the outer regions to approximately the 95% value found by stellar counts.

threshold delimits the regime where most 2MASS sources have just one counterpart in our catalogue, shown by the higher number of first neighbour correlations relative to second neighbours ones. At greater correlation distances, two catalogue counterparts becomes more likely to be found for each 2MASS source, as the number of second neighbour correlations becomes higher. Therefore, the determined threshold maximizes the matching of 2MASS sources to our catalogue ( $\sim 67\%$ ), while maintaining low levels ( $\sim 1\%$ ) of possible mismatch due to second neighbours.

Selected common sources were used to calculate a simple photometric calibration between the two datasets accounting for a zero-point magnitude difference and a linear colour correction according to the following relations:

$$J - j = j_0 + j_c (j - h) \quad (1)$$

$$H - h = h_0 + h_c (j - h) \quad (2)$$

$$K_s - k_s = k_0 + k_c (h - k_s) \quad (3)$$

where the lowercase letters represent 2MASS magnitudes, uppercase letters represent magnitudes from our catalogue,  $j_0$ ,  $h_0$  and  $k_0$  are the zero-point magnitude terms and  $j_c$ ,  $h_c$  and  $k_c$  are the colour terms. To minimize the effects of outliers, we have employed a "robust" linear fitting method and applied a simple sigma-clipping algorithm at 3-sigma. Fig. 5 shows the calibration fits of these equations over our derived aperture photometry in each filter.

Table 1 compares our fitted colour terms from aperture and PSF derived photometry with the values found by CADC<sup>1</sup>. Since uncertainties were not provided for these reference values, we inferred the 1-sigma deviation based on the FWHM of their provided colour terms distributions<sup>1</sup>. Considering these uncertainties, our aperture derived coefficients showed a good correlation with the reference values for all filters, even though the apertures used in each case were different. Although the PSF derived colour terms follow the same trends, they are significantly higher than their aperture counterpart. This is most likely due to the fact that the profile-fitting photometry is able to recover more flux from the bluer stars used in the calibration than the aperture photometry. These stars are usually close to our saturation limits presenting an extended light halo that can be easily unaccounted by the small aperture used. The

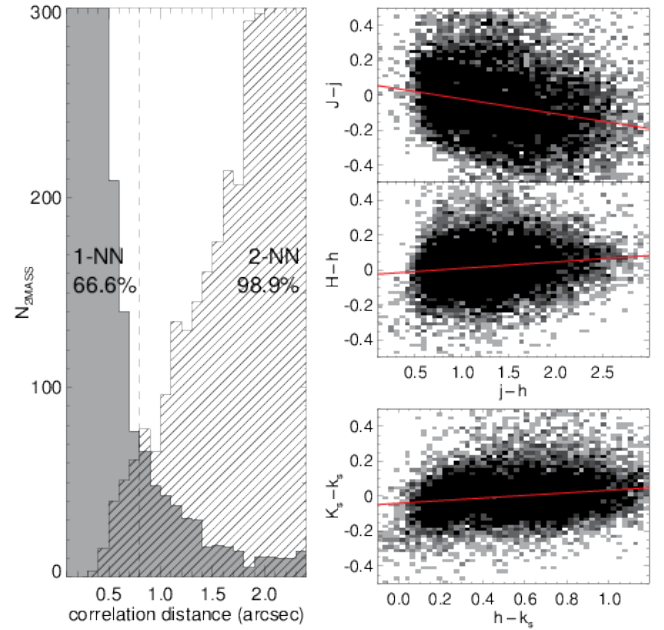


**Figure 5.** *Left:* distribution of the first (shaded histogram) and second (dashed histogram) nearest neighbour of 2MASS sources in our catalogue. The fraction of sources in each distribution with correlation distances smaller/larger than the adopted correlation threshold (dashed line) is also shown. *Right:* photometric calibration fits (solid lines) to the 2MASS catalogue in the  $J$  (top),  $H$  (middle) and  $K_s$  filters (bottom).

**Table 1.** Photometric calibration colour terms

	aperture	PSF	CADC*
$j_c$	$-0.080 \pm 0.002$	$-0.056 \pm 0.004$	$-0.064 \pm 0.017$
$h_c$	$0.037 \pm 0.002$	$0.048 \pm 0.003$	$0.031 \pm 0.009$
$k_c$	$0.075 \pm 0.003$	$0.093 \pm 0.004$	$0.058 \pm 0.026$

\* uncertainties inferred from the colour term distributions

derived zero-point magnitude terms were small, with uncertainties inferior to 0.005 magnitudes in all filters.

Since we were mainly interested in recovering bright, saturated stars to our catalogue we have opted to calibrate the 2MASS magnitudes into the WIRCcam system, instead of the other way around. Apart from being simpler as it does not involve inverting the system of equations (1-3), it also prevents the addition of the calibration errors into our photometry. Therefore, equations (1-3) were employed directly to convert the 2MASS magnitudes of stars brighter than our saturation limit into the WIRCcam photometric system. Bright stars for which the PSF fitting has not converged were also recovered from the 2MASS catalogue. Uncertainties due to the calibration were properly propagated into these stars magnitude errors; they appear as a brighter, narrower strip in the left panels of Fig. 2.

Our final catalogue thus comprises about 310000 stars spanning a 12 magnitudes range in  $J$ ,  $H$  and  $K_s$  filters and reaching  $\sim 5$  magnitudes deeper than 2MASS. It is available for download at Vizier<sup>2</sup>.

<sup>1</sup> <http://www.cadc-ccda.hia-ihh.nrc-cnrc.gc.ca/en/wirwolf/docs/filt.html>

<sup>2</sup> <http://vizier.u-strasbg.fr/viz-bin/VizieR>



**Table 2.** Catalogued clusters in the region

ID	RA (J2000)	Dec (J2000)	Ref.
LK12	20:35:22	+42:21:36	1
LK14	20:35:43	+42:29:24	1
FSR245	20:38:05	+42:13:52	2
FSR249	20:38:24	+42:30:03	2
LK13	20:38:29	+42:06:25	1
BDB60	20:38:37	+42:39:25	3
BDB59	20:38:37	+42:37:40	3
BDB58	20:38:57	+42:22:40	3
BDB57	20:39:00	+42:19:35	3
Bica3	20:40:00	+42:18:30	4
LK15	20:40:29	+42:01:48	1
BDB56	20:41:20	+41:58:22	3
BDB55	20:41:16	+41:51:51	3

<sup>1</sup> Le Duigou & Knödlseider (2002)<sup>2</sup> Froebrich, Scholz, & Raftery (2007)<sup>3</sup> Bica, Dutra, & Barbuy (2003)<sup>4</sup> Bica, Bonatto, & Dutra (2003)

### 3 CLUSTER IDENTIFICATION

The first step in analysing stellar populations is a proper identification of cluster candidates as stellar overdensities relative to the local field population, at scale lengths of a few parsecs. Confirming the physical nature of the candidate cluster members usually requires further analysis using statistical methods, colour-magnitude diagrams (CMD's) and/or spectroscopy.

Fig. 1 shows that many of the known clusters in the region (see Table 2) are often correlated with known HII regions (Paladini et al. 2003) and/or heavy 100 $\mu$ m dust emission, indicating that these stellar populations might be in their early formation stages. However, since the catalogued clusters in this region have never been studied in detail, it is not clear if they even represent coeval physical systems. Since our observations are significantly deeper than 2MASS, from which most of these clusters were identified, the previously undetected, fainter population can provide a strong constraint in determining the physical nature of these objects.

To sample the local stellar density through our field of view we have constructed stellar density charts by counting detected objects inside a flat circular kernel around each star. This produced an irregular grid on the position coordinates which was interpolated into an uniform grid. Since this approach enhances density features with dimensions similar to the kernel size, we have iterated this procedure with a range of different kernel sizes (from 10'' to 90''). The resulting density charts were then merged by median stacking the individual charts into a final density map. Fig. 6 compares two such charts built by including all stars brighter than our 95% completeness level ( $K_s < 18.5$ ) and by including only a brighter subset ( $K_s < 15.5$ ). It can be seen that although all catalogued clusters correspond to a density nearby enhancement at the brighter subset, some of them are overwhelmed by field population when the fainter population is considered, raising doubt as to the real physical nature of these objects. This is specially concerning in the identification of new cluster candidates since other uncatalogued density enhancements that seems distinguishable from the fainter population might be in fact artefacts generated by field fluctuations. Table 2 presents the coordinates of the known clusters in the region, shown in Figs. 1 and 6, with their respective literature reference.

When completeness is not an issue a real stellar cluster should present an excess of stars relative to the field, even when its fainter

population is considered. Since we are dealing with a star forming region, we do not expect severe dynamical evolution effects that could remove the fainter population of these clusters. Heavier than average extinction, however, could efficiently mask the fainter stars in some regions, making the identification of these objects very susceptible to the larger field fluctuations of the fainter magnitude population. Since our completeness levels were derived globally, we can only confirm the nature of the emerged, more populous stellar clusters that can be easily identifiable in both magnitude limited density charts shown in Fig. 6 and presenting stellar sequences in the CMD that can be clearly differentiated from the field ones. Namely, those are clusters: LK12, LK14, FSR249, LK13, BDB58, Bica3, LK15. The other objects will be considered as candidate clusters, pending a more detailed investigation on their proposed members.

### 4 PHYSICAL PARAMETERS

Although a stellar density enhancement over the field is often a prime condition for the identification of a star cluster candidate, such enhancement could easily come from statistical fluctuations of the field population, inhomogeneous extinction over the line-of-sight or incompleteness effects. Therefore, subsequent analysis of the candidate is mandatory to access the physical nature of the stellar group.

In this sense, we have applied several methods to assess the spatial structure, to derive the local visual extinction and to account for the local field population in each cluster candidate, in an attempt to uncover their physical parameters. These methods are described below as they are applied to LK12, as an example.

#### 4.1 Structural parameters

It is known that star clusters undergo a particular structural evolution during their lifetimes, evolving from a very hierarchical to a more globular structure and then expanding as they lose members, towards dissolution (e.g. Portegies Zwart, McMillan, & Gieles 2010). The timescales involved in such evolution, specially at younger ages, are very dependent on the number of stars, their spatial dimension and the gas content, but can be very short both locally and globally through the cluster (e.g. Kuhn et al. 2014; Gouliermis et al. 2012).

To characterise the structural properties of our sample, we have employed fittings of the King-Profile analytical function (King 1962) over magnitude limited radial density profiles (RDP) derived from stellar counts. For this purpose, the central coordinates of each object were updated by calculating the barycentre of the stellar sample inside 1' of the peak density value in our star density maps. A RDP was then constructed by deriving the mean stellar density inside consecutive annular bins with a constant radial bin around the centre coordinates. This procedure was iterated at different radial bin values for improved sampling. Lastly, we have used the completeness maps derived at Sect. 2.2 to perform a completeness correction to the derived RDP of our clusters, down to the  $K_{s95}$  limit. (see Fig. 4).

Fig. 7 compares the result of the King-profile fitting for object LK12, using a completeness corrected fainter sample ( $K_s \leq 18.5$ ) and a brighter stellar sample ( $K_s \leq 15.5$ ), for which incompleteness is negligible. The derived core radius, tidal radius and limiting radius (i.e. the radius at which its density profile merges with the local background) are indicated on the density maps. It can be seen that

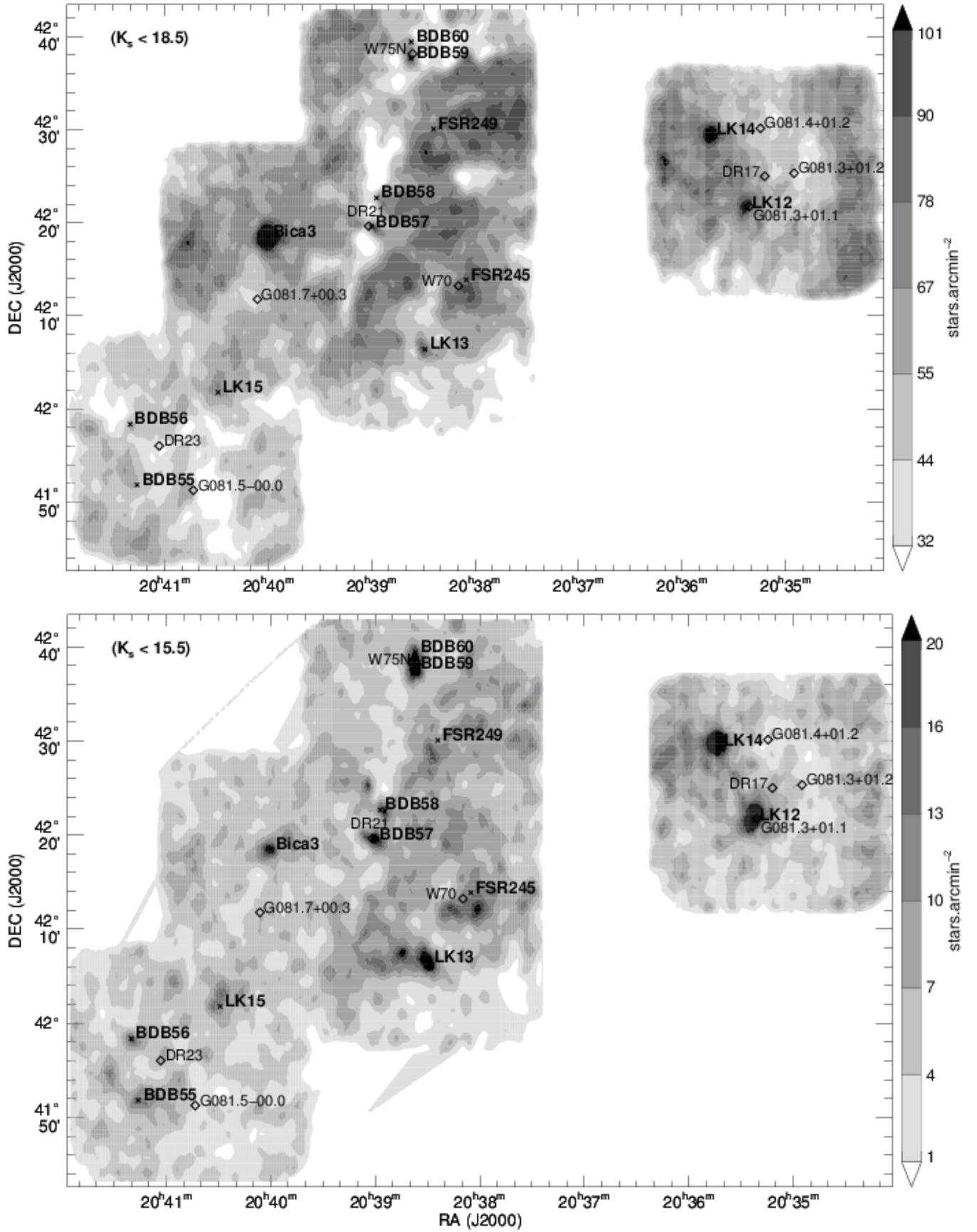


**Figure 6.** Stellar density maps of our final catalogue sampling only stars brighter than  $K_s=18.5$  (upper panel) and  $K_s=15.5$  (lower panel). Density levels are indicated by the colour bar on the right. Catalogued clusters in the region are labeled in boldfaced text and indicated by crosses. HII regions are labeled by normal text and indicated by diamonds.

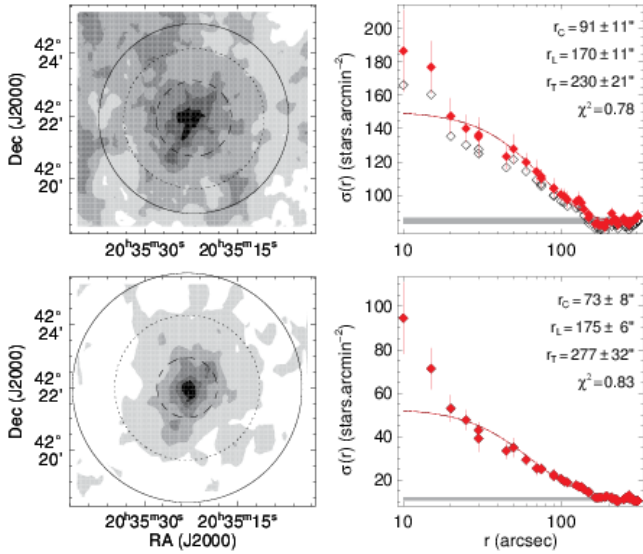


**Figure 7.** Local stellar density maps (left panels) and radial density profiles (right panels) of LK12, sampling stars with  $K_s < 18.5$  (upper panel) and  $K_s < 15.5$  (lower panel). The dashed, dotted and solid lines shown in the left panels represent the core, limiting and tidal radii, derived by the King-profile fitting (solid line) shown in the right panels. Completeness corrected sample (filled symbols with error bars) are compared to the raw sample (empty symbols).

the completeness correction is much more prominent on the fainter sample, making the distribution more peaked relative to the uncorrected sample. Furthermore, the RDP derived from the brighter stellar sample shows a reduced core radius when compared to the RDP derived from the full sample, indicating the high-mass stars are more centrally concentrated than the overall population, even when accounting for the higher incompleteness of the fainter population. This behaviour was also observed in the RDP's of BDB58 and Bica3, pointing out to a mass segregated population in these objects.

Additionally, FSR249 and LK15 presented a sub-clustered structure, which could not be described by King-like profile. However, they showed a coeval population that could be easily discerned from the field in the following CMD analysis and were therefore classified as true clusters. Their peak stellar densities were estimated from the RDP while their sizes were found by visually inspecting WIRCam images, Spitzer images and the star density maps. On the other hand, FSR245 and BDB55 presented irregular structures that were found to be field populations. For all other clusters, their derived tidal radius was used to define the cluster size.

Although source crowding was effectively quantified and corrected in these clusters, extinction heterogeneity, particularly in the central regions of BDB57 and BDB59 could bias their derived structural parameters. In this case, we expect the stellar densities derived represent lower limits, while their core radius are actually upper limits. Table 3 contains the mean stellar density ( $\bar{\rho}$ ), core radius ( $r_c$ ) and tidal radius ( $r_t$ ) for each cluster.

## 4.2 Membership

Like the majority of SFRs in the galaxy, the high extinction and relatively large distances of the stellar populations in Cygnus X makes proper motion data scarce or unavailable, impeding a kine-

matrical derivation of membership for its star clusters. In this sense, photometric based membership has proven to be a fair substitute employing a multi-colour statistical approach, often coupled to positional arguments, to characterise and separate field and cluster populations (e.g. Bonatto & Bica 2007; Froebrich et al. 2010; Dias et al. 2012; Krone-Martins & Moitinho 2014; Perren, Vázquez, & Piatti 2015). In fact, even when kinematical data is available, recent works on star cluster characterisation have been including both positional data and multi-colour photometry in a multi-dimensional analysis to better constraint their derived memberships (e.g. Sánchez & Alfaro 2009; Sarro et al. 2014).

In our membership analysis we adopted the photometric method devised in Maia, Corradi, & Santos (2010), which assigns pertinence values to stars based on the local stellar density difference between a contaminated cluster sample and a control field sample in a multi-colour space according to the relation

$$P_{phot} = \frac{\rho_{clu} - \rho_{fld}}{\rho_{clu}}, \quad (4)$$

where  $\rho_{clu}$  and  $\rho_{fld}$  represents the local stellar density in the cluster and field samples, respectively, taken at the same position in the multicolour space. The method can also benefit from a 1-D positional argument representing the distance to the cluster centre to weight its assigned membership probabilities and better remove contaminants. The process is robust to the field sample selection as long as it is representative of the contaminating population in the cluster region. Generally, we have adopted the tidal radius as a limit to the cluster population and an annular ring around it with the same area as the inner region as the field sample, except when an inhomogeneity (e.g. another cluster or a dense cloud) is present. In such cases a manual selection of cluster or field region is often preferred.

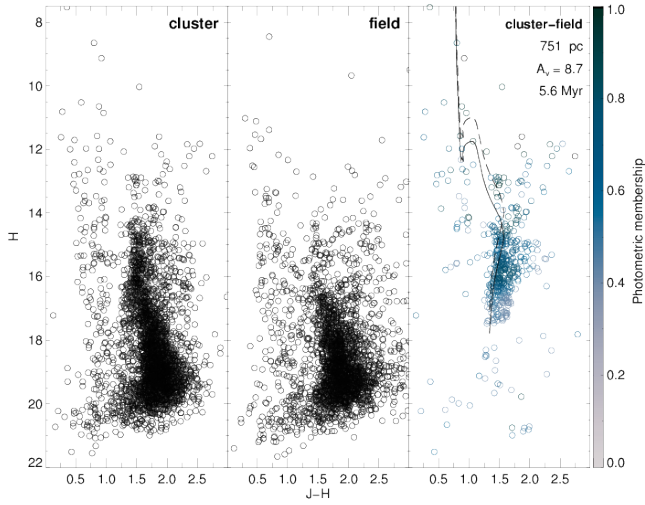
Once a cluster and a field sample are supplied, a member list is readily defined from the derived membership probabilities by adopting a suitable cutoff threshold. Previous work with the method with a large and diverse cluster sample (Maia, Piatti, & Santos 2014) has shown that a cutoff at 30% to 50%, depending on the level of field contamination, is optimal to clearly reveal cluster sequences in the CMD.

Fig. 8 shows the result of such procedure comparing the cluster, field and the decontaminated sample of LK12, projected in the  $H$  vs  $J-H$  CMD. Although some outlying contaminants are still present, the method has been able to successfully separate most of the visible cluster sequence.

## 4.3 Extinction

Since most SFR present large quantities of the parental cloud gas and dust, modelling extinction has become a crucial step in studying these regions, particularly through photometric data. In this sense, near-infrared data has been playing a crucial role as it can reach significantly deep in these gas rich environments and most importantly due to its availability through several ground-based surveys (e.g. 2MASS, VISTA) and observing facilities.

To this end, far-optical to mid-infrared colour excesses have been used in conjunction to known extinction laws to derive extinction maps in SFR spanning a diversity of spatial scales (e.g. Lombardi, Alves, & Lada 2006; Scandariato et al. 2011; Majewski, Zasowski, & Nidever 2011). While this approach may underestimate extinction in the most obscured areas (due to the absence of stars beyond the obscuring cloud), the derived values are often well correlated to CO maps, which are regarded as good tracer of cold,



**Figure 8.** CMD comparing the samples in LK12 region (left panel), in its nearby field (middle panel) and the field-subtracted sample (right panel). The colour bar shows the assigned photometric probabilities. Isochrones representing the single star (solid line) and equal mass unresolved binaries (dashed line) populations are shown, along with the most probable age, distance and extinction inferred.

dense clouds and does not require additional data (HI, dust emission) other than the stars photometry.

Since our sample is expected to be composed by a coeval population of pre main sequence low mass stars, down to  $\sim 0.1 M_{\odot}$ , we have refrained from adopting a fixed intrinsic colour value or relying on calibrated intrinsic colours for our extinction calculations, since these are more appropriate for dwarf stars of later spectral types. Instead we have opted to use the intrinsic colours derived from stellar evolutionary models for solar metallicity stars.

Although many models are currently available in the literature, we have found that very few provide tracks for pre-main-sequence stars (PMS) covering stellar masses from  $\sim 0.1$  to possibly  $10\text{--}50 M_{\odot}$ , namely the model by [Siess, Dufour, & Forestini \(2000\)](#), hereafter SDF00 reaching  $7 M_{\odot}$  and the model by [Bressan et al. \(2012\)](#), hereafter PARSEC), reaching over  $300 M_{\odot}$ . Fig. 9 compares the PARSEC isochrones of ages from 1 to 10 Myr in the  $H \times J-H$  and  $J-H \times H-K_s$  diagrams. It can be seen from the colour-colour diagram that for such young ages, that the overall colour excess differences arising from such large age uncertainties ( $\Delta \log t = 1.0$  dex) would be very small possibly reaching  $\Delta(J-H)_0 \sim 0.1$  in certain mass domains. In addition, the CMD shows that different aged PMS populations could theoretically be discerned, even in the absence of giant stars, due to the increasing colour extent between the main-sequence turn in point and the reddest turn around  $\sim 0.5 M_{\odot}$  ( $J-H \sim 0.7$ ), possibly tied to the developing of a radiative core. However, these differences would require a colour resolution inferior to  $\sim 0.2$  mag at the relatively faint red turn.

Given a particular model isochrone, we have used the extinction law of [Rieke & Lebofsky \(1985\)](#) to constrain the slope of the reddening vector in the colour-colour diagram and find the isochrone intercepts that define the intrinsic colours of a particular star. As shown in Fig. 9, most of our stars will intercept the isochrones at two different points, corresponding to a stellar mass smaller/greater than  $\sim 0.7 M_{\odot}$ . Afterwards, extinction estimative to each of these intercepts can be easily calculated through one of the

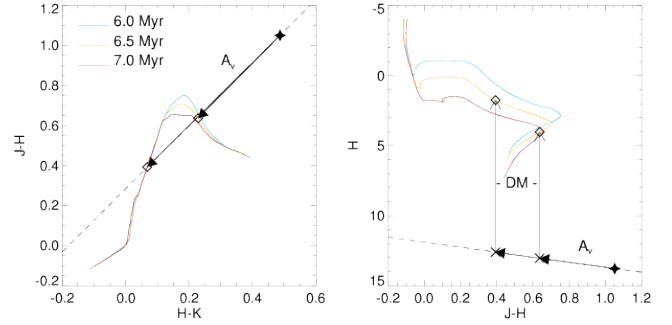


**Figure 9.** Colour-colour (left) and colour-magnitude (right) diagrams comparing solar metallicity isochrones of  $\log t$  6.0, 6.5 and 7.0. It shows how the reddening vector (dashed lines) can be used to derive both the extinction and distance modulus for a particular star, given its possible isochrone intercepts (diamonds).

following relations:

$$A_v^{jh} = 9.725 \times E(J - H) \quad (5)$$

$$A_v^{hk} = 15.314 \times E(H - K_s) \quad (6)$$

$$A_v^{jk} = 5.948 \times E(J - K_s) \quad (7)$$

For most stars these equations return identical values, as expected. However, we have opted to use the extinction derived from  $J$  and  $H$  bands (first equation) as they are less likely to be affected by infrared colour excess, shown more strongly in  $K_s$  band. Moreover, these bands provide a larger colour difference between the lower and higher mass isochrone intercepts (see Fig. 9), which makes easier the determination of the right intercept.

As a byproduct of using isochrones for determining the intrinsic colours, distance modulus for each intercept can also be determined through one of the following equations:

$$DM^j = J - J_0 - 0.28765 \times A_v \quad (8)$$

$$DM^h = H - H_0 - 0.18482 \times A_v \quad (9)$$

$$DM^k = K_s - K_0 - 0.11952 \times A_v \quad (10)$$

As with the extinction, these equations returns very close values for most of stars, save for a few presenting  $K_s$  band excess. To avoid these cases we have adopted the median of such values for improved accuracy.

Extinction uncertainties were evaluated for by properly propagating the photometric errors through equations (5–7). Likewise, distance modulus uncertainties were calculated by taking into account both the photometric and extinction uncertainties for a star. Note that these errors are invariant, whatever choice is made regarding the isochrone intercepts of a particular star.

Since a smooth extinction solution is often expected through these young populations, determination of the 'best' isochrone intercept for each star can be done through a global minimisation of the extinction dispersion. This was done in a two-step process in which all stars were initially assigned to its lowest possible extinction values (corresponding to lower mass isochrone intercept) and later iterated through their possible extinction values to find the configuration that minimises the dispersion of the whole sample. Note that although this configuration also constrains a 'best' distance modulus for each star, it usually does not minimizes the dispersion of the distance moduli.

Once such configuration was found an extinction probability density function (PDF) was built for each star using its 'best' in-



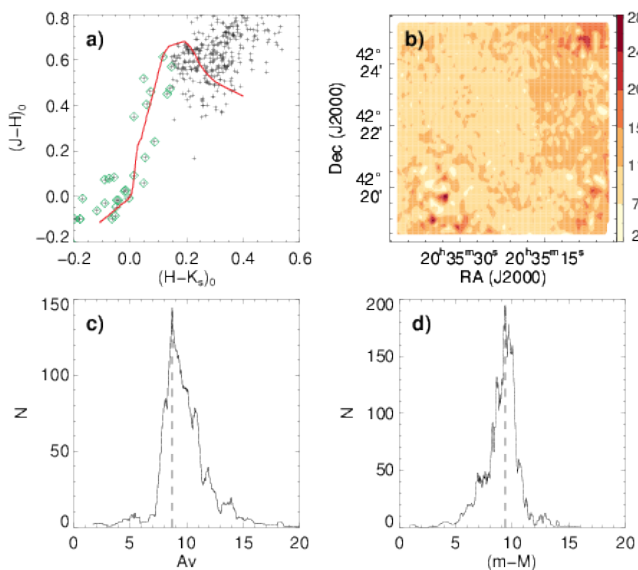


**Figure 10.** Results of the extinction determination showing (a) the adopted isochrone (solid line) and the intrinsic colours of LK12 stars, dereddened using the expected extinction value for the population. Most stars (plus signs) were assigned to their lower mass intercept in the isochrone while a few bluer ones (diamonds) were assigned to the higher mass intercept. The derived extinction values were interpolated into a local extinction map (b), with the colour bar indicating the extinction levels, and used to construct the global extinction (c) and distance modulus distributions (d) for LK12 stars from which their expected values (dashed lines) were derived.

ferred extinction value and assuming a normal distribution of its uncertainty. A global extinction distribution was then created by stacking the individual extinction PDF of each star. The expected extinction value for the population was finally estimated as the peak value of this global extinction distribution. Similarly, a global distance modulus distribution was also derived and an expected distance modulus value evaluated from its peak.

Fig. 10 shows the result of such procedure over the stars in the vicinity of LK12. It can be seen that the inferred 'best' isochrone intercepts have successfully matched most of the stars to the lower mass domain of the isochrone in the colour-colour diagram, while assigning slightly bluer stars to the higher mass interval, providing a good dereddening solution for the cluster population. An extinction map was promptly derived from the full local stellar sample by interpolating their extinction values into an uniform grid with a desired ( $5''$ - $15''$ ) resolution.  $A_v$  and DM distributions, in the other hand, are best derived from a field-cleaned sample, in order to increase the statistical significance of the cluster population and improve the determination of their expected values.

Although small fluctuations can be seen through the global extinction distribution, it is clear that the population shows a very pronounced peak value with positively skewed tail. This means that the expected extinction value actually represents the minimum extinction towards the population, or the foreground extinction shared by a larger fraction of stars. Intra cluster extinction is often variable and therefore won't form secondary peak in the distribution, but will produce the observed tail towards larger extinction values.

#### 4.4 Distance and age

Even though extinction can be well constrained through the stars colours, determination of distance and age of a stellar population through photometry is met with several difficulties as many phenomena can displace the stars from their fiducial position in the CMD. Intra-cluster nebosity and variability (which may arise intrinsically or due to surrounding material) are likely the most unaccounted effects. These are, however, somewhat attenuated on populous objects as they are likely to be better sampled across the mass spectrum and to possess a greater population of stars in their 'right' position in the CMD from which the parameters can be more reliably determined.

In this context, several methods have been developed recently to reliably determine ages from CMD data using a variety of approaches such as statistical indicators, bayesian inference and synthetic populations (e.g. Jørgensen & Lindegren 2005; Naylor & Jeffries 2006; Monteiro, Dias, & Caetano 2010). Although many of these methods can lift the known degeneracies between some isochrone parameters (e.g. age-metallicity, reddening-age), they are often not optimised to deal with pre-main-sequence populations showing very heterogeneous stellar distribution over the CMDs.

In our approach, although neither the derived extinction distribution nor its expected value are expected to change considerably with the adoption of different aged isochrones, it is very likely that the distance modulus distribution will (see Fig. 9). In order to determine which isochrone best describes a particular population we have adopted a strategy very similar to the one used for deriving extinction, seeking to minimize the dispersion of distance modulus distribution across a range of ages. This was quantified by defining a coefficient to be maximised, that measures how sharp the extinction and distance modulus distributions derived from a particular isochrone are. It was defined as:

$$S(\log t) = \left[ \frac{N_{max}}{W} \right]_{A_v} \times \left[ \frac{N_{max}}{W} \right]_{DM} \quad (11)$$

where  $N_{max}$  represents the peak value and  $W$  the FWHM of either the extinction ( $A_v$ ) or distance modulus ( $DM$ ) distribution derived from a particular isochrone.

Such method provides an advantage over curve-fitting or synthetic CMD techniques in the sense that it is very robust to outliers such as bright field stars since they will show a range of unrelated extinction and distance modulus values that will not disturb the contained distribution of the dominant stellar population.

The procedure described on the last section was then repeated for the full range of solar metallicity PARSEC isochrones aged from 1 Myr to 1 Gyr and the corresponding  $S$  coefficient determined for each one of them. This was also done using the solar metallicity SDF isochrones from 1 Myr to 100 Myr, taken at the exact same ages as the former ones. Fig. 11 compares the normalised  $S$  coefficients as a function of age for the first three objects of our list. It can be seen that both isochrone models provides  $S$  peaks at compatible ages, within a 0.2 dex margin, with the PARSEC tracks showing a smoother solution, possibly due to its larger mass coverage and finer sampling across the mass spectrum.

A most probable age interval was then defined as the region around the  $S$  peak, taken from the PARSEC isochrones, where the  $S$  values showed an enhanced value over the local 'pseudo-continuum' distribution (see Fig. 11). For our objects this interval spanned an age range inferior to 0.4 dex, which most of the time corresponds to an uncertainty of 0.2 dex around a central value. This uncertainty is about the same order as the one arising from

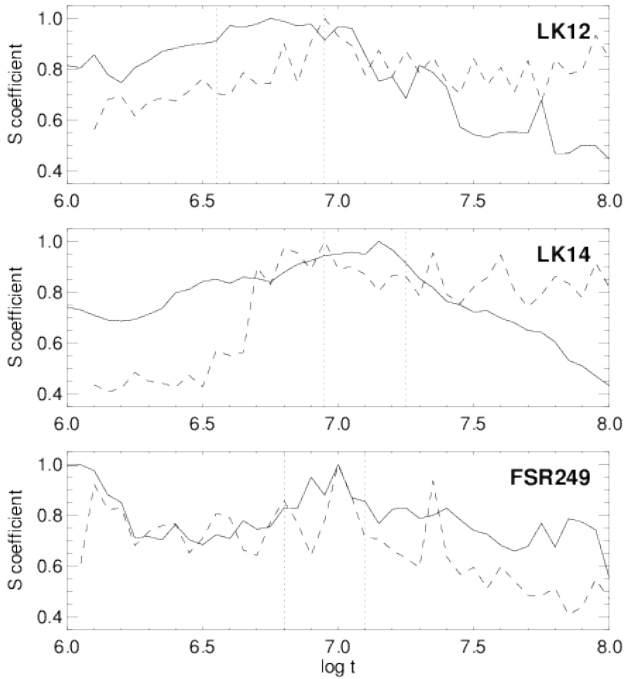


**Figure 11.** Normalised  $S$  coefficients derived from SDF (dashed lined) and PARSEC (solid line) isochrones spanning 1-100 Myr for objects LK12, LK14 and FSR249. The most probable age interval adopted for each object is indicated by the vertical dotted lines.

the adoption of different isochrone models. Combining these values would result in a general age uncertainty of  $\sigma_{\log t} = 0.28$  dex.

The isochrones corresponding to the derived age interval are likely to produce very similar extinction distributions while producing distance modulus distributions peaked at different values. As Fig. 9 shows, the youngest isochrone is likely to constrain the maximum distance modulus value, with the oldest one constraining the minimum value. Therefore, we have used the range of expected distance moduli derived from these isochrones to determine a most probable distance interval for each object. For LK12, the cluster presenting the largest probable  $\log t$  range in our sample ( $6.55 \leq \langle \log t \rangle \leq 6.95$ ), the expected (peak) distance moduli have shown values between 9.08-9.58 mag while the expected (peak) extinction values varied between 8.69-8.82. This would translate into a most probable distance interval between 655-825 pc and into an extinction uncertainty of only  $\sigma_{A_V} = 0.07$  mag.

The derived most probable values of age, distance and extinction were used to superimpose the single-star sequence and that corresponding to equal-mass unresolved binaries over the CMD of LK12, shown in Fig. 8. The model sequences appears to be in good agreement with the loci of the cluster stars.

#### 4.5 Mass distribution

There is ongoing debate of whether star formation follows a universal mass distribution - described by the initial mass function (IMF) (e.g. Kroupa et al. 2013; Chabrier 2005) - or if it can be affected by the properties of the local environment. Although there is growing evidence showing that the IMF appears to be constant across different SFRs and even in the sub-stellar regime (Bastian, Covey,

& Meyer 2010; Offner et al. 2014), the matter is not settled (e.g. Treyer et al. 2011; Dib 2014).

In this sense, the distribution of stellar masses in open clusters is probably the most used method to investigate the IMF due to the advantages in studying a coeval population: uniform distances, ages and reddening. Embedded young clusters provide even more appealing subjects, as they allow sampling of more massive stars and due to the fact that their mass distribution may have not had the time to dynamically process or evolve, thus being closer to its true initial conditions.

Derivation of stellar IMF is usually difficult, especially in young populations. Apart from the usual problems in dealing with obscured regions, it also requires knowledge of mass-luminosity relationships appropriate for pre-main-sequence phase, which are currently scant. Since we are employing PMS stellar models to characterise our stellar populations, once a particular model has been found to best reproduce an observed sample, the stellar masses can be derived from the isochrone mass-luminosity relationship.

In order to achieve that, the star's apparent magnitudes were converted to their absolute values using the most probable extinction and distance modulus derived for the population. Furthermore, the uncertainties in these parameters (see previous section) were properly added to the photometric errors to calculate realistic uncertainties for the absolute magnitudes. Assuming a normal distribution of these uncertainties, a monte-carlo procedure was then employed to construct a binned  $M_J$  luminosity function which was afterwards corrected for the local incompleteness, as derived from our artificial star simulations (see Fig. 4). The isochrone mass- $M_J$  relationship was then used to convert this completeness corrected luminosity function and its monte-carlo derived uncertainty to a mass distribution, with stars fainter/brighter than the isochrone mass limits being discarded. Again, PARSEC isochrones were preferred due to their largest mass coverage ( $0.1 \leq m(M_\odot) \leq 350$ ). Fig. 12 shows the luminosity and mass functions derived from the assigned members of LK12.

A log-normal analytical IMF function from Chabrier (2005), hereafter refereed as the IMF, was fitted to the computed mass function to derive a characteristic mass ( $m_c$ ), mass dispersion ( $\sigma_m$ ) and high-mass power-law exponent ( $\alpha$ ) for the distribution, through the following relations:

$$\xi(m) = \frac{dN}{dm} = \frac{A}{m} \exp \left[ -\frac{(\log m - \log m_c)^2}{2\sigma_m^2} \right], \quad m \leq 1 M_\odot \quad (12)$$

$$= A k m^{-\alpha}, \quad m \geq 1 M_\odot$$

where  $A$  and  $k$  are normalisation constants. The fit was limited in the fainter domain by either the 95% completeness limit or by faintest luminosity bin where the cluster sequence could be clearly identified in the CMD.

We have also adopted its parametrisation of the galactic field system IMF as reference values:  $m_c = 0.25 \pm 0.05$ ,  $\sigma_m = 0.55 \pm 10$  and  $\alpha = 2.35 \pm 0.36$ , where the uncertainty of the first two parameters were arbitrarily set to 20% level, due to their absence. These reference values and their uncertainties were used, along with the normalisation (and its uncertainty) derived for each cluster, to define a domain in the mass distribution plot inside which stars are said to comply with the IMF. This was meant to provide an uncertainty derived scatter around the nominal IMF parameters. Both the fitted function and the derived IMF compliance domain are shown in Fig. 12.

Total stellar mass and its uncertainty was also estimated by summing contributions from individual mass bins. This was also done by assuming a population composed entirely of equal mass

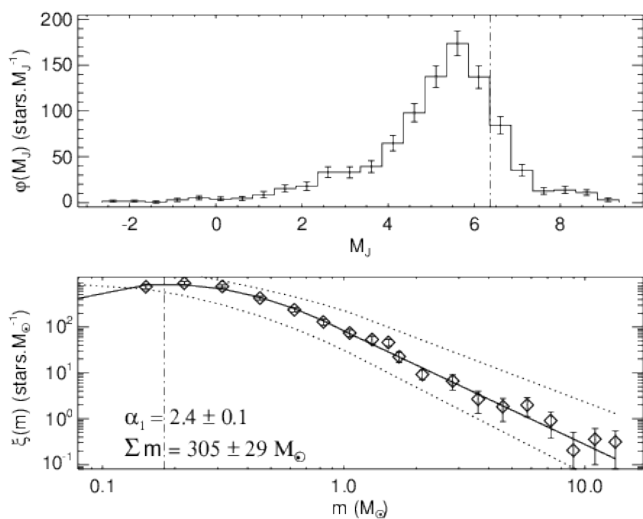


**Figure 12.** Completeness corrected  $M_J$  luminosity function (top) and corresponding mass function (bottom) of LK12. Error bars indicate the monte-carlo derived uncertainty (see text). The vertical dot-dashed lines indicate the fainter limit of the mass function fitting range. The solid line indicates the best fit to a log-normal mass-function while the dotted ones delimit the reference IMF domain. The derived total mass and the fitted high-mass exponent are shown.

unresolved binaries (i.e. shifting the derived luminosity function by 0.75 mag and doubling the star counts). Since the difference between such estimates were larger than the  $\sim 10\%$  uncertainty derived in each case, we have instead reported the total cluster mass as a range where the lower limit corresponds to the mass derived from the single star (unmodified) population and the upper limit corresponds to the mass derived for a population of binaries. The true cluster mass is likely to be in between.

In addition, whenever a region smaller than the derived cluster size had to be used in the analysis (i.e. due to a nearby feature or object), a correction factor was calculated from the ratio of the expected number of stars inside this region to the expected total number of stars inside the cluster tidal radius, and applied to the derived total mass. These expected numbers of stars were obtained by integrating the cluster analytical King profile function through the appropriate domains. For example, we have restricted the analysis of LK12 to its inner  $173''$  due to nearby nebulosity, even though its computed tidal radius was  $252''$ . Integration of its King profile in the inner region yields 454 stars, comparable to the decontaminated sample of 449 stars, used in the analysis. Integration up to its tidal radius yields 473 stars, implying that about 96% of its total stellar population was sampled in the inner region. Therefore, a correction factor of  $1/0.96$  was applied to its derived mass to compensate for the unaccounted population in the outer region of the cluster.

## 5 INDIVIDUAL RESULTS AND COMMENTS

The methodology described in Sect. 4 was employed to study the catalogued objects in the region. Previous literature references and potential comments on the analysis of each object are given in this section. For most of the clusters image cuts from our NIR mosaics are compared to Spitzer image cuts taken from the processed mo-

saics of the *Cygnus-X Spitzer Legacy Survey*<sup>3</sup> downloaded from NASA/IPAC Infrared Science Archive (IRSA). A compilation of the most important physical parameters derived is shown in Table 3, including the mean stellar density ( $\bar{\rho}$ ), the core ( $r_c$ ) and tidal ( $r_t$ ) radii, the mean extinction ( $A_v$ ) and the mass function characteristic mass ( $m_c$ ), mass dispersion ( $\sigma_m$ ) and high mass slope ( $\alpha$ ). Objects FSR245, BDB55 and BDB60 are not shown, as we have found the former two to not represent physical systems and could not reliably determine the parameters of the latter.

Although some of our targets have been previously processed by Kharchenko et al. (2013, hereafter K13) pipeline we have found that many of their derived parameters are at odds with the ones determined in this work. Because proper motion in the Cygnus-X region is mostly unavailable or unreliable, their analysis relied heavily on 2MASS photometric data, often extracted in regions many times greater than the clusters projected size with scant numbers of probable members. Furthermore, it appears that for the majority of young clusters (those lacking a turn-off), age could only be estimated by eye fitting of an isochrone. Therefore, although comparison with their results are provided, we found that they might be unreliable for young, very reddened and/or compact objects, like many of our targets.

### 5.1 LK12

LK12 is frequently referred as DR17 IR cluster, given its proximity to this bright radio source and HII region. The compact X-ray source AXJ2035.4+4222-Src2 lying on the centre of the cluster was found to be probably associated with Cygnus Rift at  $d \leq 1.0$  kpc (Roberts, Romani, & Kawai 2001), being the strongest constraint to the cluster's youth and distance. Although two spectroscopic confirmed OB stars could be found in the cluster periphery, their derived extinctions differ significantly from the cluster mean value, suggesting that they might belong to the field. Indeed, one of them (TYC 3159-6-1) was reported as a runaway B1 supergiant with  $A_v=5.9$ , age of 4.0-4.5 Myr and distance between 1.2 and 1.5 kpc (Gvaramadze et al. 2014), while the other (TYC 3161-106-1) was reported as a Cygnus OB2 field B1III star with an age of 14 Myr,  $A_v=3.7$  and distance of 1.4 kpc (Comerón & Pasquali 2012).

The Spitzer composite image shown in Fig. 13 reveals the presence of a pillar-like structure beyond the southeast border of this cluster that appears to point north, towards LK14, while being ionised from the northwest. Although LK12 lies closer to the pillar, the direction of nearby cometary tails reveals that the region is being ionised by the brighter stars at the center of DR17, approximately  $5'$  northwest. CO emission velocity channel maps by Schneider et al. (2006) seems to suggest that W75N and DR17 are somewhat connected, as their emission peaks at the same velocity channels. This was also found by G12 which assigned a distance of 1.0-1.8 kpc to both regions.

Dutra & Bica (hereafter, DB01 2001) were the first to identify this cluster assigning a visual extinction of 15 and a distance of 1.2 kpc. It was later revisited by LK02, who reported a visual extinction between 9-18 and a distance between 1.3-2.0 kpc. Furthermore, an integrated mass estimative of 600-1760  $M_\odot$  was calculated by extrapolating a fitted high mass slope of  $\alpha=2.61 \pm 0.25$ . Both works have used 2MASS data and relied on general M/L relations to derive the cluster physical parameters rather than directly

<sup>3</sup> <https://www.cfa.harvard.edu/cygnus-X/>

**Table 3.** Derived physical parameters for clusters and candidates

ID	RA ( $^{\circ}$ : $^{\circ}$ : $^{\circ}$ )	Dec ( $^{\circ}$ : $^{\circ}$ : $^{\circ}$ )	$\bar{\rho}$ ( $\text{pc}^{-2}$ )	$r_c$ (pc)	$r_t$ (pc)	Age (Myr)	$A_v$	D (kpc)	Mass ( $M_{\odot}$ )	$m_c$ ( $M_{\odot}$ )	$\sigma_m$ ( $\log M_{\odot}$ )	$\alpha$
LK12	20:35:22	42:21:54	174 $\pm$ 18	0.29 $\pm$ 0.02	0.92 $\pm$ 0.07	4-9	8.73 $\pm$ 0.07	0.65-0.83	318-441	0.34 $\pm$ 0.04	0.34 $\pm$ 0.02	2.44 $\pm$ 0.10
LK14	20:35:42	42:29:31	274 $\pm$ 40	0.23 $\pm$ 0.03	0.84 $\pm$ 0.10	9-18	8.49 $\pm$ 0.04	0.92-1.12	433-621	0.38 $\pm$ 0.13	0.30 $\pm$ 0.04	2.08 $\pm$ 0.10
FSR249	20:38:29	42:29:15	100 $\pm$ 39	0.44 $\pm$ 0.19	0.93 $\pm$ 0.33	7-13	7.00 $\pm$ 0.12	1.45-1.75	312-458	0.38 $\pm$ 0.19	0.39 $\pm$ 0.08	1.83 $\pm$ 0.11
LK13	20:38:29	42:06:22	922 $\pm$ 101	0.08 $\pm$ 0.01	0.25 $\pm$ 0.01	4-6	7.19 $\pm$ 0.06	0.45-0.55	38-46	0.20 $\pm$ 0.06	0.35 $\pm$ 0.03	1.98 $\pm$ 0.34
BDB59	20:38:37	42:37:29	77 $\pm$ 17	0.18 $\pm$ 0.03	0.72 $\pm$ 0.11	1-3	12.95 $\pm$ 0.03	1.15-1.38	224-274	0.22 $\pm$ 0.12	0.50 $\pm$ 0.09	1.41 $\pm$ 0.32
BDB58	20:38:54	42:22:44	46 $\pm$ 6	0.40 $\pm$ 0.10	1.30 $\pm$ 0.10	1-3	13.47 $\pm$ 0.06	2.74-3.34	610-772	0.30 $\pm$ 0.10	0.37 $\pm$ 0.07	1.53 $\pm$ 0.29
BDB57	20:39:02	42:19:37	117 $\pm$ 63	0.04 $\pm$ 0.01	0.40 $\pm$ 0.15	1-3	24.40 $\pm$ 0.06	0.60-0.78	163-218	0.18 $\pm$ 0.10	0.46 $\pm$ 0.07	1.36 $\pm$ 0.12
Bica3	20:40:01	42:18:17	12 $\pm$ 1	1.34 $\pm$ 0.11	3.85 $\pm$ 0.25	$\sim$ 500	15.10 $\pm$ 0.03	4.49-5.10	$\sim$ 3000	—	—	1.33 $\pm$ 0.14
LK15	20:40:30	42:03:13	70 $\pm$ 22	0.44 $\pm$ 0.16	1.02 $\pm$ 0.28	1-3	11.18 $\pm$ 0.18	1.65-2.13	367-475	0.55 $\pm$ 0.26	0.33 $\pm$ 0.11	1.67 $\pm$ 0.10
BDB56	20:41:19	41:58:09	97 $\pm$ 22	0.15 $\pm$ 0.01	0.58 $\pm$ 0.06	2-5	9.80 $\pm$ 0.13	1.39-1.61	140-186	0.41 $\pm$ 0.18	0.40 $\pm$ 0.08	1.79 $\pm$ 0.11

determining an age for the cluster. This cluster was also processed by K13, reporting an age of 4 Myr,  $A_v=10$  and distance of 1.7 kpc.

Our results point out that LK12 is a young (4-9 Myr) emerging ( $A_v \sim 9$ ) cluster and that it lies closer than reported by previous studies, at a distance of 650-825 pc. These parameters would imply a diameter of 1.8 pc, and a stellar mass distribution that appear to be consistent with the one by LK02 in the high-mass range and that follow the IMF down to 0.2  $M_{\odot}$ , totalling 315-440  $M_{\odot}$ . Because of a heavy extinction column in its eastern region, the analysis of this cluster was based in a reduced sample, extracted at a inner radius (173'') rather than at its tidal radius (252''). Integration of its derived King-profile reveals that this reduced sample corresponds to  $\sim 96\%$  of the sample expected at its tidal radius. Therefore, the reported total mass estimative has been corrected by this factor, assuming a homogeneous mass distribution. The main charts involved in this cluster analysis are compiled in Fig. A1.

## 5.2 LK14

LK14 is located about 8' north of LK12 and could also be related to D17 SFR, given their proximity. Its stellar population, as seen in Fig. 13, appears considerably more evolved than LK12, presenting less extinction and being composed of fainter stars with a more centrally condensed distribution than its neighbour. Its central star has been spectroscopically observed by Rawlings, Adamson, & Whittet (2000) and classified as a O7-B9.5 star with  $A_v=9.2\pm 0.3$ .

This cluster was first identified by LK02, acknowledging it as an evolved, nearby object with  $A_v \sim 8.5$ . They derived a tentative spectral type for the bright central star, obtaining B0 or O5.5 whether the assumed distance was about 800 or 1250 pc, finally adopting the latter result and rejecting the central star as a foreground object. An integrated mass estimative of 470-1160  $M_{\odot}$  was also calculated by extrapolating a fitted high mass slope of  $\alpha=2.51\pm 0.35$ .

We have found this cluster to be significantly older than its neighbour presenting an age between 9-18 Myr,  $A_v=8.5$  and distance between 920-1120 pc. These parameters would imply a 1.7 diameter cluster with a stellar mass distribution that is consistent with the one by LK02 in the high-mass range and that appears to follow the IMF down to 0.3  $M_{\odot}$ , totaling 430-620  $M_{\odot}$ . Concerning the brightest star in the center of the cluster, we have used the Rawlings, Adamson, & Whittet (2000) optical B and V magnitudes for this star along with Carroll & Ostlie (2006) stellar calibrations and our derived distance modulus and extinction to estimate an spectral type B0-B1 for this star. This is in accordance with the mass estimate of  $\sim 14 M_{\odot}$  given by the adopted isochrone models for our

JHK<sub>s</sub> photometry. Since that this star also shows a extinction that is very consistent with the cluster mean value, we believe that it does belong in the cluster and might have held an important role in shaping the local environment in DR17. The main charts involved in this cluster analysis are compiled in Fig. A2.

## 5.3 FSR245

This cluster candidate was identified by Froebrich, Scholz, & Raftery (2007) by using stellar density counts from 2MASS catalogue. It was later included in one of the regions analysed by Beerer et al. (2010) around the "diamond ring" (see Sect. 5.5), reporting it to be relatively older than the surrounding regions. It lies close to the radio source W70, and features a bright blue star with considerable 24 $\mu$ m emission that appears to have cleared out the gas and dust around it. Despite that, the region appears featureless both in our WIRCam and Spitzer images (Fig. 14), presenting a highly fragmented stellar distribution that is not compatible with a King-profile.

Our analysis has found two most probable age peaks centred around 10 Myr and 500 Myr for this object. However, these peaks are much broader than found for the other analysed clusters indicating that they do not represent coeval populations, representing instead two overlapped field populations with very different mean ages. The stellar extinction and distances also present bimodal distributions with an abundant, exposed ( $A_v \sim 3$ ) population at 1.2 kpc and a highly reddened ( $A_v \sim 11$ ) one at much greater distances, possibly related to background Galactic arms. Although they can be identified on the CMD, none of these two populations show any spatial correlation, both being dispersed over the field.

We conclude that FSR245 is not a real cluster, but instead a region inside the "diamond ring" that has been cleared out of the local dust and gas content by a nearby massive star, thus allowing for the emergence of the background population of the Galactic disk. That is probably the cause of the local stellar density enhancement that led to the initial identification of this object.

## 5.4 FSR249

This cluster candidate was identified by Froebrich, Scholz, & Raftery (2007) and subsequently processed by K13, classifying it as a large (10 pc), young (1 Myr) and emerged ( $A_v \sim 4$ ) cluster at 1.8 kpc. Fig. 15 shows that although it is hard to distinguish it from the rich background on our images, its brighter population is better constrained in Spitzer frames revealing it to be inside a gaseous



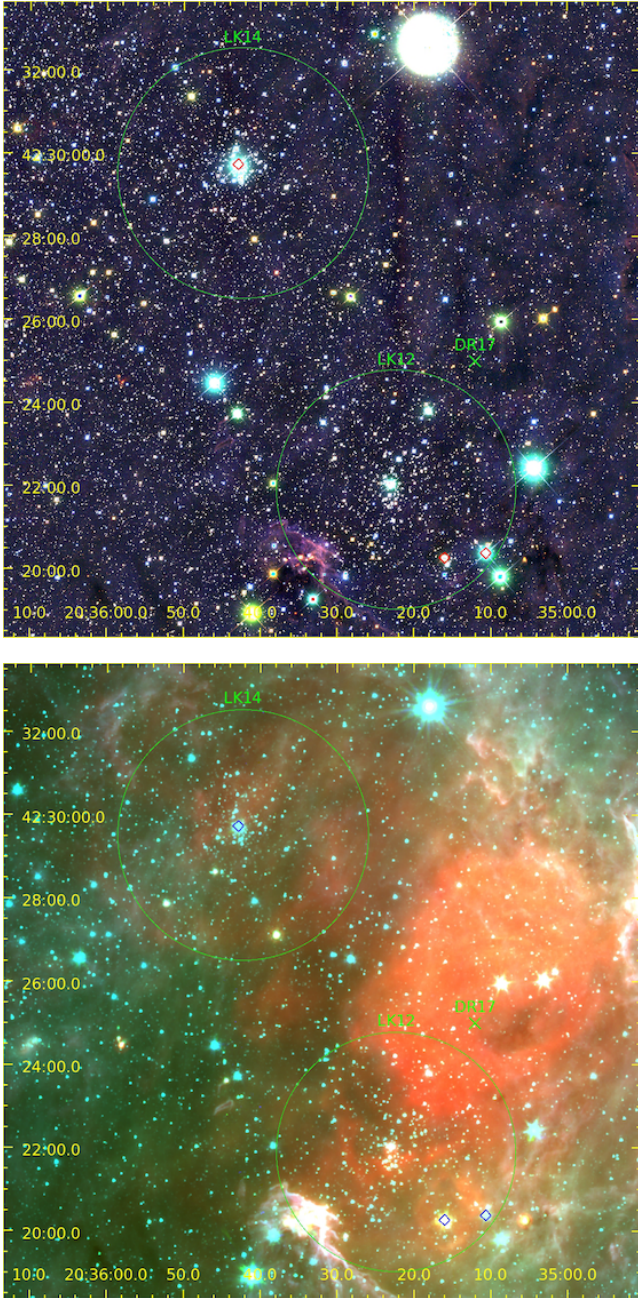


**Figure 13.** Colour-composite images of the region around DR17, as seen from our  $J$ ,  $H$  and  $K_s$  images (top) and from Spitzer [3.6], [4.5] and [24] $\mu\text{m}$  channels (bottom). The extraction radius for LK12 and LK14 are indicated, along with nearby, known B-type stars (diamonds).

filament extending irregularly to the northwest but converging towards DR21 SFR, about southeast. Star density maps of FSR249 shows that although it presents a dense central clump, it still does not have a globular-like shape and therefore converged very poorly to our King-profile fittings. Therefore, we have arbitrarily defined a  $\sim 2'$  radius (close to the derived tidal radius of  $110''$ ) based on the visual inspection of the stellar density maps and on the extent of the gaseous structure seen on its Spitzer image.

Our analysis have found two age ranges that are equally probable at 1-2 Myr and 7-13 Myr. Although the younger one appears to

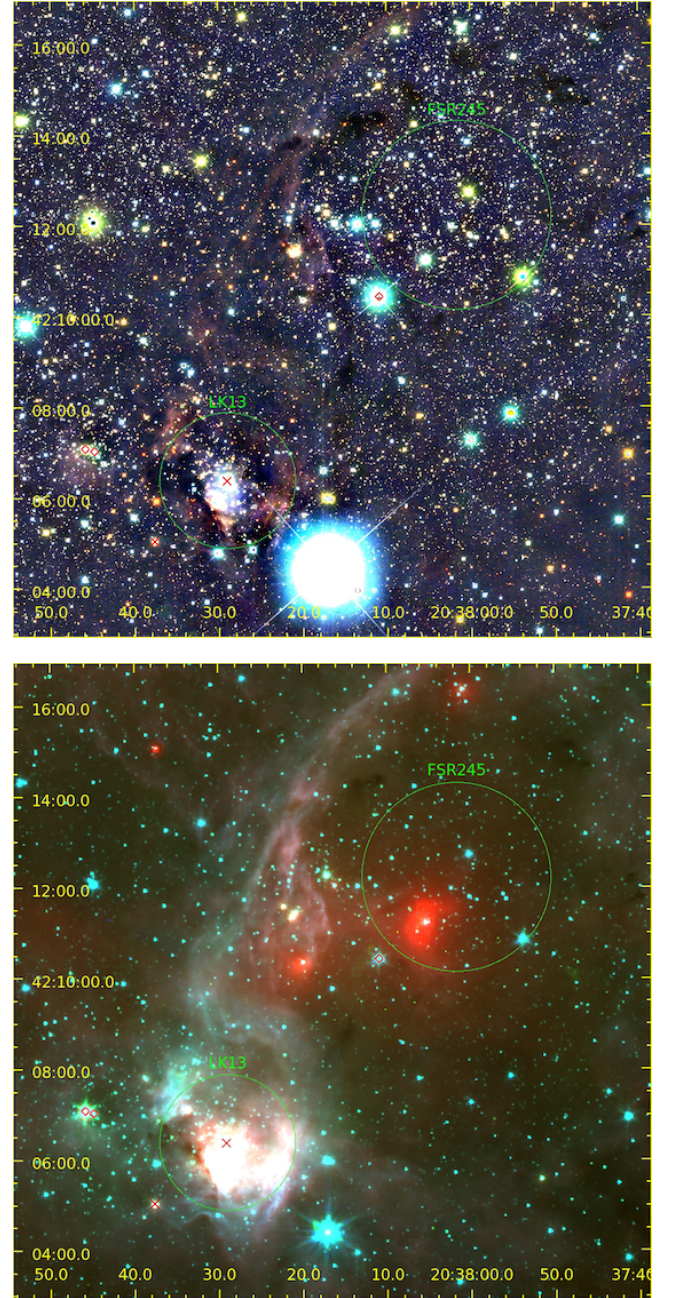


**Figure 14.** Colour-composite images of the region around the "diamond ring", as seen from our  $J$ ,  $H$  and  $K_s$  images (top) and from Spitzer [3.6], [4.5] and [24] $\mu\text{m}$  channels (bottom). The extraction radius for FSR245 and LK13 are indicated, along with nearby, known B-type stars (diamonds) and K0 stars (crosses).

be in agreement with the age by K13, we believe that the older age range found seems to be more in accordance with the loose population and relatively lower extinction ( $A_v=7.0$ ) found in FSR249. This choice would put this object at a distance of 1.4-1.7 kpc which is somewhat closer than reported by K13 but compatible with distance estimates for the SFR DR21 by G12 and R12, reinforcing the idea that these two objects might be related.

At this proposed distance, FSR249 is a parsec sized cluster ( $\sim 2$  pc diameter) with a well populated pre-main-sequence that



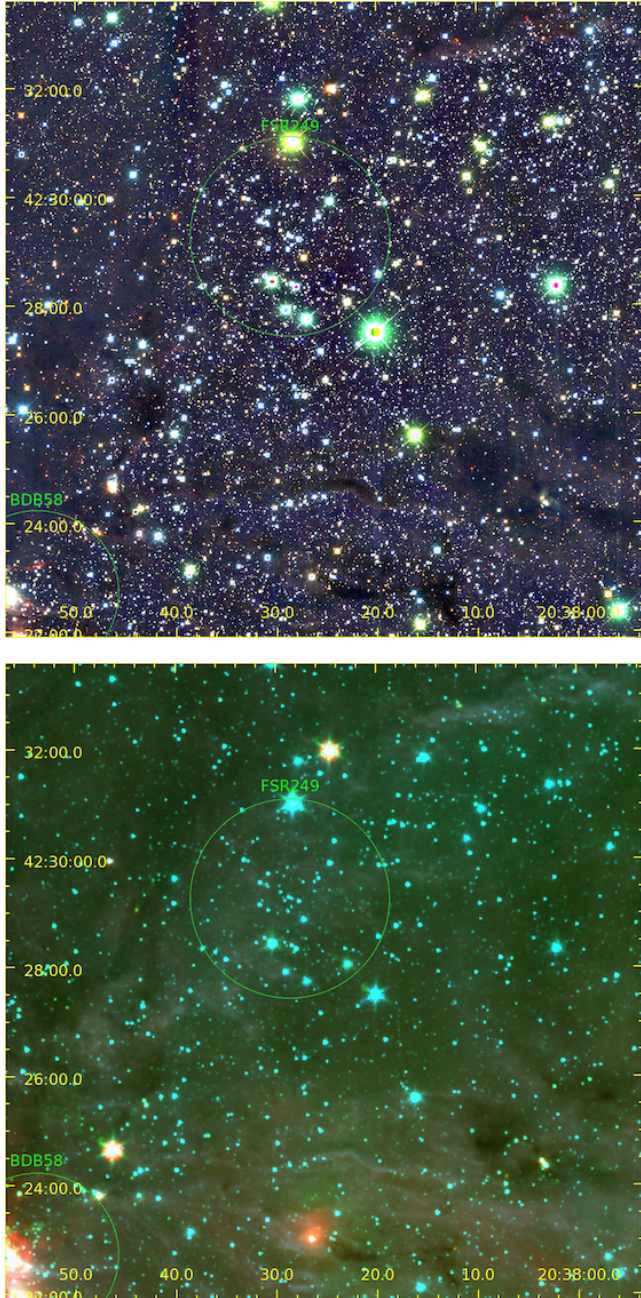


**Figure 15.** Colour-composite images of the region between FSR249 and DR21, as seen from our *J*, *H* and *K<sub>s</sub>* images (top) and from Spitzer [3.6], [4.5] and [24] $\mu$ m channels (bottom). The extraction radius for FSR249 is indicated in the figure.

appears to contain a high fraction of binaries. Its stellar population sums up to 310-460  $M_{\odot}$ , with a distribution that barely follows the IMF, showing a consistent excess of high mass stars down to  $\sim 1 M_{\odot}$ . On the other hand, assuming the younger age range would put this cluster at 2.8-3.2 kpc with a total mass of 936-1375  $M_{\odot}$  and a diameter of 3.4 pc. The main charts involved in this cluster analysis are compiled in Fig. A3.

## 5.5 LK13

LK13 resides at the southern tip of the "diamond ring", a gaseous ring-like structure powered by a central HII region, which appears to be connected to the DR21 (approximately 15' northeast) by filaments (Marston et al. 2004). However, inspection of the composite Spitzer image shown in Fig. 14 reveals that while LK13 appears to be illuminating and ionising the neighbouring southern and western gas structures, there is no such indication for the northern gas structure, which forms the diamond ring.

This object was first identified by DB01 and later confirmed as a cluster candidate by LK02 which assigned a minimum visual extinction of  $\sim 9$  and predicted the presence of 12 B stars in the cluster region, assuming a distance compatible of the Cygnus OB2 association ( $\sim 1.6$  kpc). Subsequent work by Beerer et al. (2010) has acquired spectra of 536 massive star candidates in Cygnus-X, finding only two nearby B-stars, largely outside the projected radius of LK13, but also reporting two very bright K0 stars inside its tidal radius, one being in the very centre of LK13.

There is little doubt that LK13 is a real, emerging ( $A_v \sim 7$ ) cluster. Although our analysis have found two equally probable age ranges of 4-6 Myr and 9-13 Myr, the prevalent gas content points to the younger value which corresponds to a distance of 450-550 pc, much closer than previously thought. Based on these results we estimate that the most massive stellar object near the centre of this cluster has 2-4  $M_{\odot}$ , which is in rough agreement with its early K-type spectra found by Beerer et al. (2010), if one considers the high binary fraction expected to be found in the central region of the cluster.

These results would picture it as a compact cluster ( $\sim 0.5$  pc diameter) in a foreground layer of the complex associated with the Cygnus Rift molecular cloud, found at a distance of 500-800 pc by G12. Its stellar population sums up to 40-45  $M_{\odot}$  and appears to follow the IMF, albeit unreliable at the high mass end due to poor statistics. On the other hand, adoption of the older age range would lead to a much shorter distance of 320-400 pc, implying a smaller diameter (0.3 pc) and total mass (32-37  $M_{\odot}$ ). The main charts involved in this cluster analysis are compiled in Fig. A4.

## 5.6 BDB60

This object was first identified as a cluster by DB01 and classified as a resolved pair to BDB59. However, even though it is separated from BDB59 by only  $\sim 2'$ , it appears substantially different from its neighbour. Spitzer images shown in Fig. 16 reveals that it presents much less emission in the longer wavebands and that its stellar content is almost completely exposed, suggesting a more evolved evolutionary stage. Moreover, although BDB60 bright stars are projected very close to the very embedded BDB59, they show no evidence of interaction with its massive gas content, indicating they could reside in distinct layers (i.e. the foreground) of the cloud complex instead of being associated with BDB59. Indeed, early CO mapping of this region by Cong (1977) has found gaseous structures associated with W75N that appears to belong to Great Cygnus Rift rather than being related to the DR21 complex to the south.

Due to the scarcity of stars and extinction heterogeneity, we could not reliably determine the physical parameters for this candidate cluster. Although we have found that its spatial distribution is consistent with a king-profile with a tidal radius of  $74''$ , close to the initial size estimate by DB01, the poor statistics precludes a definite conclusion on its nature, as such profile could very well arise from a random gathering of a few field stars.



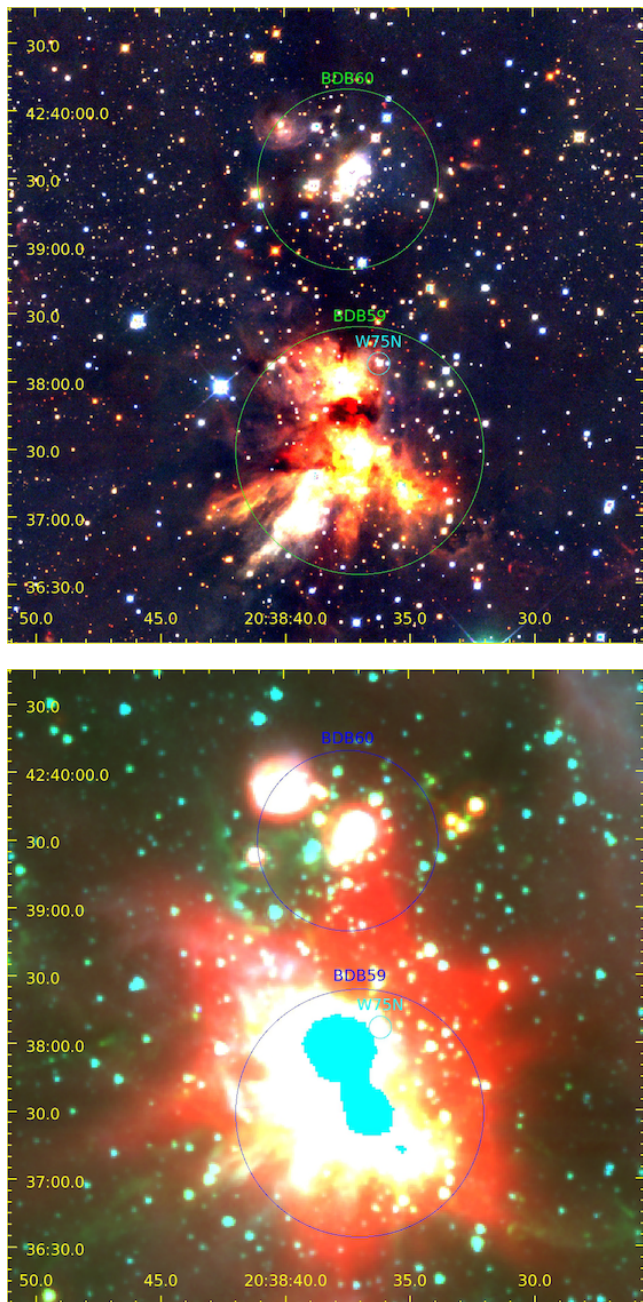


**Figure 16.** Colour-composite images of the region around W75N, as seen from our  $J$ ,  $H$  and  $K_s$  images (top) and from Spitzer [3.6], [4.5] and [24] $\mu$ m channels (bottom). The extraction radius for BDB59 and BDB60 are indicated in the figure.

### 5.7 BDB59

This stellar cluster is coincident with the well studied SFR W75N which has been resolved into at least three radio sources (Hunter et al. 1994), possibly associated with ultra-compact HII regions and water masers found in the vicinity (Torrelles et al. 1997). Recent observations in the mid infrared (Persi, Tapia, & Smith 2006) and millimetre (Shepherd, Kurtz, & Testi 2004) wavebands have shown that these are probably excited by still embedded early B-type protostars aged from 1 to 5 Myr. Parallax measurements by R12 have constrained a distance of  $1.30 \pm 0.07$  kpc for W75N while CO mea-

surements by G12 has found an emission layer at 1.0-1.8 kpc for this SFR, possibly overlapping (but not interacting) with a background layer related to DR21 in the south.

In order to reduce contamination from nearby BDB60 object (see Fig. 16), we have limited our analysis to the inner 55'' of this object. Although this aperture is large enough to encompass all radio and HII sources previously detected in this SFR, our photometry cannot reach the deepest, embedded sources, thus being more biased towards the revealed, outer population. Nevertheless, we have estimated from its fitted King-profile that this sample correspond to  $\sim 88\%$  of the one at its tidal radius and have adjusted the derived total mass accordingly.

Although still plagued by contamination and highly variable extinction, our analysis shows that most stars comprises a young (1-3 Myr), embedded (minimum  $A_v = 13.5$ ) star cluster at a distance of 1.1-1.4 kpc. Using its tidal radius as a size indicator would result in an actual diameter of 1.4 pc. The total stellar mass amounts to 220-270  $M_\odot$  with a distribution does not seems to follow the IMF in the high-mass end, showing a excess of massive ( $m > 5 M_\odot$ ) stars. In this sense, the reduced radius used in the analysis could be effectively filtering out lower mass stars in the cluster outer region, if its stellar content is mass segregated. The main charts involved in this cluster analysis are compiled in Fig. A5.

### 5.8 BDB58

This massive emerging cluster was first identified by DB01 and lies close to the DR21(OH) source, located at the northern tip of a gaseous ridge that extends towards the main body of DR21, about 3' to the south. SCUBA dust-continuum mapping by Davis et al. (2007) has found this gaseous structure extends further north into a filamentary structure, and suggested a likely distance of 3.0 kpc for the entire complex. Methanol maser kinematics by Pestalozzi, Minier, & Booth (2005) constrains a similar distance for the northern ridge of DR21 based on two sources, one of which lies inside BDB58 radius.

Fig. 17 shows that although it appears more extended and completely embedded in the Spitzer image, part of its western side has already emerged revealing a very red stellar population in our near-infrared image. The ridge and gaseous filaments can be seen as dark lanes in our images.

Our results points out that this is an emerging cluster probably younger than 2.5 Myr, presenting a minimum  $A_v = 13.5$  and residing at a distance of 2.7-3.3 kpc. At this distance its tidal radius would translate into a diameter of 2.6 pc. Although an exponent is given, its stellar mass distribution does not appear to follow the IMF at high mass end ( $m > 1 M_\odot$ ) showing an excess of high mass stars, and summing up to 610-770  $M_\odot$ . The main charts involved in this cluster analysis are compiled in Fig. A6.

### 5.9 BDB57

This nascent cluster, often identified as W75S or DR21 IR cluster (Hodapp 1994), lies in the centre of DR21, the most studied SFR in the Cygnus-X north complex. However, although a multitude of radio and IR studies revealed several clumps, molecular jets, masers and YSO's in this region, a definitive distance is still lacking. Many early studies (e.g. Campbell et al. 1982) and more recent ones (e.g. Davis et al. 2007) have been favouring distances up to 3 kpc, largely based on kinematical data and galaxy rotation models. Recent maser parallaxes by R12 have found 1.5 kpc, based



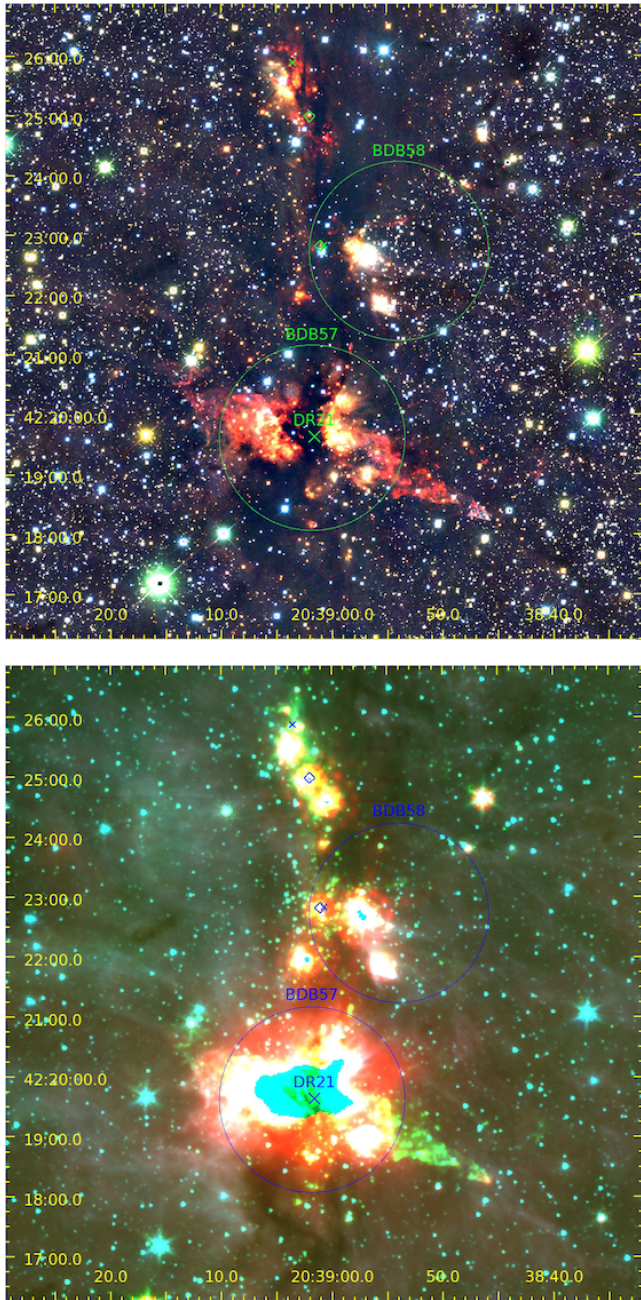


**Figure 17.** Colour-composite images of the region around DR21, as seen from our  $J$ ,  $H$  and  $K_s$  images (top) and from Spitzer [3.6], [4.5] and [24] $\mu$ m channels (bottom). The extraction radius for BDB57 and BDB58 are indicated, along with nearby masers used for distance estimation via parallax (diamonds) and kinematics (crosses).

on three sources residing largely in the northern ridge (see Fig. 17), while CO emission maps by G12 puts it between 1.5-2.5 kpc.

Presenting the largest extinction found among our sample (minimum  $A_v=24.4$ ), we have only been able to provide tentative parameters for BDB57, given its scant population and large extinction heterogeneity. The most probable age found ( $\sim 1.4$  Myr) is very close to the minimum age sampled by our method (1.0 Myr), suggesting that it could have been limited by our sampling. The corresponding distance (assuming a 1.0-1.4 Myr age) is 600-800 pc and

should be regarded as a minimum threshold since the adoption of a younger age would certainly reflect in an increased distance modulus (see Fig. 9). Based on these parameters, the cluster diameter would be 0.8 pc with a stellar population amounting to 160-220  $M_\odot$  that appear to follow the IMF in the low mass range, but not in the high mass ( $m > 1 M_\odot$ ) regime. Again, given the distance uncertainty, these should be regarded as minimum thresholds.

Although our tentative distance modulus is much smaller than previous findings, it's not unrealistic to expect an increase of one magnitude (leading to a distance of  $\sim 1.3$  kpc) for a 0.6 Myr aged system. However, given our data, we find it impossible to reach values as high as 2.0 kpc. In addition, previous distance estimates for the BDB57 cluster are not very well constrained as they were either carried over globally, through the gas/dust component of the whole DR21 complex, or punctually, over a few maser sources at least  $4'$  away from the stellar cluster centre, well outside its derived tidal radius. In fact, [Hanson, Luhman, & Rieke \(2002\)](#) has found that two radio sources in the very center of DR21, for which no distance estimate has ever been made, have no counterpart in the NIR, presenting only extended nebular emission that does not originate in the radio sources either. They conclude that these sources might be completely unrelated to the star formation traced in the NIR. Since we cannot say if this is the case for the BDB57 cluster, the derived cluster parameters of this cluster remains tentative ones, at best. The main charts involved in this cluster analysis are compiled in Fig. A7.

### 5.10 Bica3

This object was first classified as a possible distant and old physical system by [Bica, Bonatto, & Dutra \(2003\)](#) based on the identification of a CMD sequence that resembles a giant branch. Although featureless on Spitzer images, our images show Bica3 as a rich and compact population of faint stars approximately  $15'$  east of DR21 complex.

Our analysis indicates that Bica3 is indeed a very reddened ( $A_v=15.1$ ) and old (450-630 Myr) open cluster probably residing at the background Perseus arm (distance 4.5-5.0 kpc), corroborating the initial guess on this object nature. These parameters would imply a diameter of 7.7 pc at its tidal radius and a total stellar mass of  $\sim 3000 M_\odot$ , leading to a surprisingly big open cluster for its age. Its mass distribution shows a very flat spectrum, probably due to left-over contaminants at brighter magnitudes and/or incompleteness at the fainter end.

We should note that the total mass for Bica3 is probably overestimated. The actual observed mass function sums up to  $\sim 1600 M_\odot$  sampling the mass range between 1-3  $M_\odot$ . The extrapolation of the mass function to lower masses to account for the 'unobserved' stars was done using the fitted power law slope of  $1.3 \pm 0.3$  rather than the canonical value of 2.3, and can be highly dependent on the normalisation adopted and the involved star counts. A leftover field population would be substantially enlarged when extrapolating star numbers into the low mass domain. In that matter, although the field decontamination procedure employed could successfully account for the abundant population in the local arm, its performance in sampling and removing the obscured field population of the Perseus arm in the background is much more reduced. The main charts involved in this cluster analysis are compiled in Fig. A8.



### 5.11 LK15

This object was identified by LK02 and reported as being possibly associated with DR23, approximately 10' southeast. Although a stellar density enhancement is discernible in our NIR image (Fig. 18), specially at brighter magnitudes, it is hard to assign a clear circular border to this object as the presence of various foreground dust lanes gives it a very structured appearance in the NIR. Since King-profiles could not reliably describe its stellar density profile, we have instead turned to the brighter stellar content ( $K_s < 15.5$ ) density charts to derive its structural parameters. Although the resulting parameters are likely to represent the higher mass stellar content, our derived tidal radius ( $\sim 2'$ ) is considerably smaller than the  $\sim 7'$  adopted by LK02, which is large enough to include several gaseous filaments and nearby dark ridges along with the exposed stellar group.

Despite its youth (1.0-3.0 Myr) LK15 appears to be an emerged population ( $A_v=11.5$ ) at a distance between 1.7-2.1 kpc, consistent with the estimated value for DR23 (2.0 kpc, Odenwald & Schwartz 1993). One very bright star at its centre and presenting compatible extinction (there is a second bright, but much redder star) could be responsible for clearing away the gas and producing an ionisation front at its south border, seen in the Spitzer images. Our derived parameters and the colour calibrations by Knödlseeder (2000) suggests it to be a late O-type star and the used isochrone tables gives a  $\sim 70 M_\odot$  star. In addition, our results imply a physical diameter of 2.0 pc and an expected stellar mass of 370-485  $M_\odot$ , showing a small excess of high mass stars ( $m > 1 M_\odot$ ) when compared to the IMF. The main charts involved in this cluster analysis are compiled in Fig. A9.

### 5.12 BDB55

This candidate cluster was identified by DB01 and assigned as being probably associated with the DR23 radio/HII region approximately 4' northwards. Since the work by LK02, it has been misidentified in the SIMBAD database as their object 15 (LK15 in this work), located  $\sim 15'$  to the northwest. It has also been processed by K13 (object #3395), deriving an age of 2.5 Myr,  $A_v \sim 6.5$  and distance of 4.2 kpc. However, we find it hard to describe any stellar population in Cygnus with these parameters since a much higher reddening would be expected from such young, distant stellar group.

Spitzer imaging of BDB55 (Fig. 18) shows that it is characterised by a small clumping of bright stars that appears to be right inside a filamentary, ionised structure extending from a gaseous complex in the west. However, our NIR images reveals that the bright stars that compose this object are in fact, foreground blue sources, superimposed on a very reddened population inside the gaseous structure.

In fact, we have found that this object most likely does not correspond to a physical system. It does not show any density enhancement over the background in the fainter magnitude domain and its bright star clumping does not correspond to a King-profile distribution. Moreover, the faint stellar population in the area are very similar to that of the nearby field, being completely decimated in the our field removal analysis. The leftover bright stars showed very small extinction and a vertical structure on the CMD typical of the upper main-sequence stars.

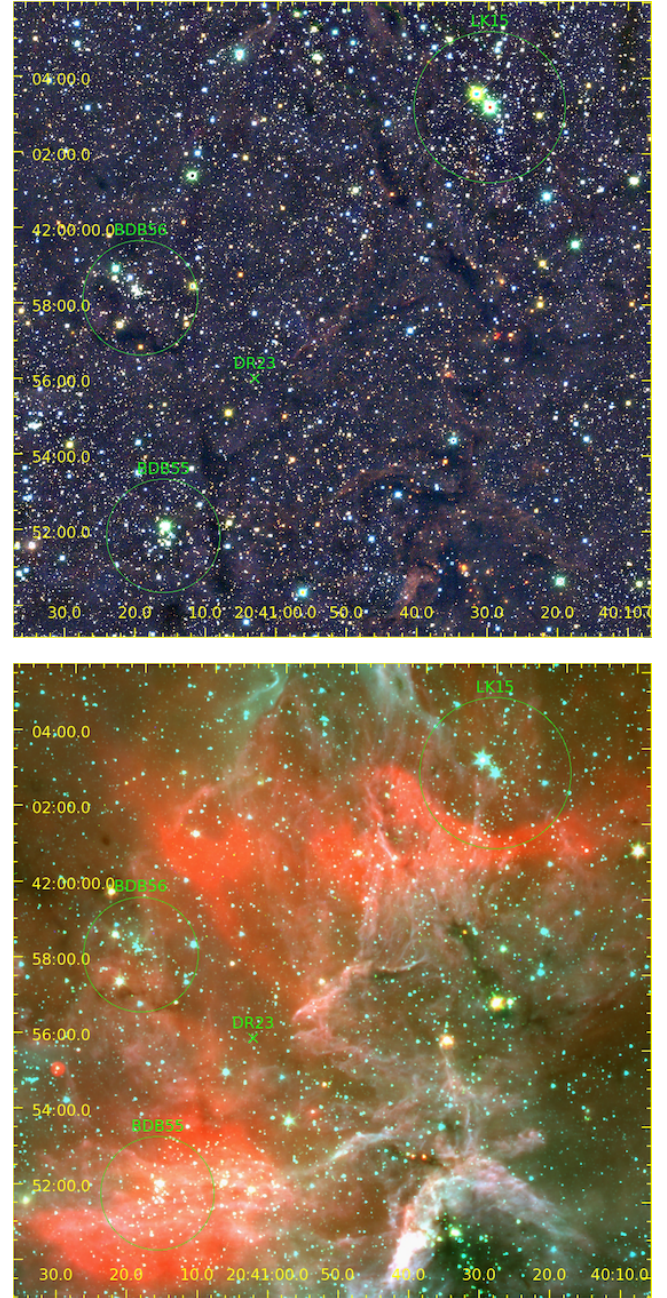


**Figure 18.** Colour-composite images of the region around DR23 (marked with an X), as seen from our  $J$ ,  $H$  and  $K_s$  images (top) and from Spitzer [3.6], [4.5] and [24]  $\mu\text{m}$  channels (bottom). The extraction radius for LK15, BDB55 and BDB56 are indicated.

### 5.13 BDB56

This object was found by DB01 and was also assigned to be possibly related to the nearby DR23 region, about 3' southwest. Processing by K13 (object #3396) have derived an age of 800 Myr,  $A_v \sim 5$  and distance of 1.2 kpc. For such small stellar numbers, these parameters would correspond to a remnant or dissolving old cluster among Cygnus predominantly young population. Although possible, we believe their results might have been misguided by the very reddened (but still young) field stars.

Fig. 18 shows BDB56 as a very noticeable star clustering in

both the Spitzer and our NIR images. Dark lanes are also visible in the cluster vicinity, probably associated with foreground clouds in Great Cygnus Rift as they do not seem to be interacting in any way with the local, bright stellar content. Overall, the intra-cluster region appears to be devoid of gas, suggesting a more evolved evolutionary state. A bright blue star near its centre has been spectral typed as a A7 star with very small extinction ( $A_V=3.9$ ) by Beerer et al. (2010). Our photometry and the colour calibrations by Knödlseeder (2000) gives this star a distance of approximately 630 pc, compatible that of the foreground Cygnus Rift.

Our analysis have shown that BDB56 is a young (age 2-5 Myr), emerged cluster ( $A_V=9.8$ ) at a distance of 1.4-1.6 kpc, indicating that it might not be associated with DR23 if a 2.0 kpc distance is assumed for this radio source. At our derived distance, this cluster has 1.2 pc diameter with a total stellar mass of 140-190  $M_\odot$  with a distribution compatible with the IMF, albeit showing an slightly excess of massive stars. Furthermore, our results points out that brightest star in the vicinity has reddening compatible with the cluster population and is probably a B0-B1 star according to the color calibrations by Knödlseeder (2000). The main charts involved in this cluster analysis are compiled in Fig. A10.

## 6 GENERAL RESULTS AND DISCUSSION

### 6.1 Embedded cluster properties

Concerning the low-mass, log-normal domain of the IMF ( $m < 1 M_\odot$ ), the clusters in this region presented similar mass distributions, showing a mean characteristic mass of  $m_c=0.32\pm0.08 M_\odot$  and a mean mass dispersion of  $\sigma_m=0.40\pm0.06$ . Fig. 19 compares their individual mass functions with reference values from the Pleiades, Hyades and Blanco 1 clusters (Moraux et al. 2003, 2007). It is clear that the IMF characteristic mass appears to be robustly constrained around 0.3  $M_\odot$ , while the mass dispersion appears to present larger variations between the different regions. In this sense, our mass distributions are narrower than those found for the Pleiades and Blanco 1, ( $\sigma_m=0.52$ -0.58) but agrees very well with the value derived for the old Hyades cluster ( $\sigma_m=0.38$ ). However, when compared to these clusters, our sampled masses are generally one decade shallower presenting only one or two reliable mass bins fainter than the log-normal peak (i.e. the characteristic mass). A proper consideration of the brown dwarf population in each cluster should be done to better constraint these parameters, particularly the mass dispersion.

By analysing the clusters structural parameters, we have found that the sizes of all young objects are well constrained at the one parsec scale, with most diameters ranging from  $\sim 1$  pc to 2 pc. Although being considerably smaller than evolved open clusters, their derived concentration parameters ( $2.0 \leq r_t/r_c \leq 4.0$ ) agree very well with the values typically observed in these older clusters (e.g. Sánchez & Alfaro 2009). In addition, taking into account their masses and assuming a virialised population, their calculated velocity dispersions (i.e.  $\sigma_v = \sqrt{GM/r}$ ) amount to  $\approx 2$  km/s for all clusters, also in agreement with values generally found in older open clusters. This is remarkable, considering that the we are sampling much younger clusters distant from 0.5 to 3.0 kpc across at least three different SFRs, and puts strong constraints into their very early structural configuration.

In addition, the derived mean stellar densities ( $\bar{\rho}$ ) seems to indicate that the older star clusters (age  $> 4$  Myr) are, on general, slightly denser than the younger ones of the same mass range (e.g.

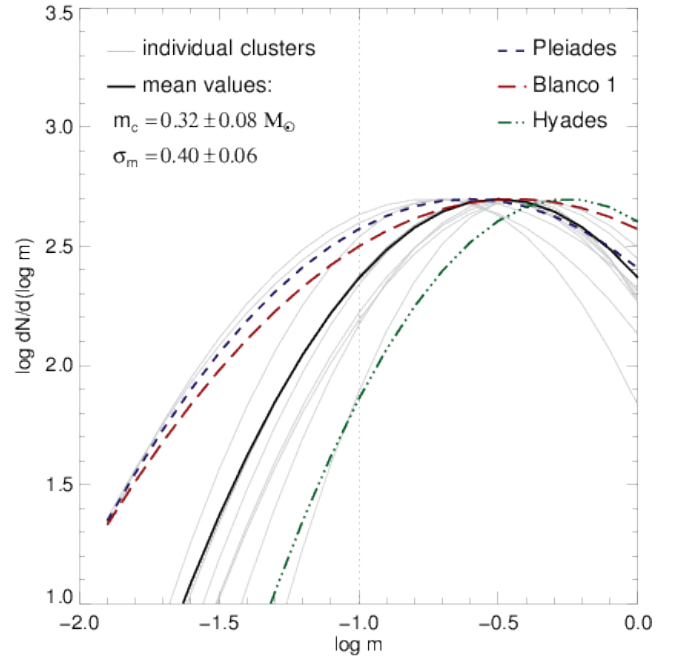


**Figure 19.** Comparison of the individual (thin lines) and mean (thick line) log-normal mass functions derived in this work with the reference values (dashed lines) for the Pleiades, Blanco1 and Hyades clusters. The vertical dotted line represent the minimum mass sampled in our IMFs ( $0.1 M_\odot$ ).

LK12, FSR249 and LK15), contrary to the expected evolutionary behaviour of stellar populations. However, given the very early age of our youngest clusters, it could be wondered whether they are fully formed systems or if one could still expect an enlargement of their stellar population due to ongoing star formation, accretion from the nearby SFR or simply emerging from its parental cloud as the gas is dissipated. In this sense, it is clear from our derived extinctions that most of our clusters under  $\sim 4$  Myr are still embedded and thus able to enhance their overall stellar densities over the next few Myr.

An observed trend between the clusters age and mass function slope at higher masses ( $m > 1 M_\odot$ ) might be related to a similar issue. The younger clusters present a shallower slope with respect to the IMF while older ones show steeper distributions, compatible with the IMF nominal value ( $\alpha=2.35$ ). Given the early age and highly embedded state of the younger clusters, it is unlikely that they have lost their lower mass content due to dynamical evolution. Therefore, it could be argued that these clusters populations either do not follow the IMF or were not sampled at a appropriate spatial scale to properly populate the observed IMF. In this sense, it is possible that some of their low mass content, formed in its outer regions, might not have had the time to sink to their central regions where our stellar samples were extracted. Indeed, consideration of the large gas content inside these objects would greatly increase their (stellar derived) tidal domain, allowing them to draw stars from much farther away on the SFR into the forming cluster. This would support a scenario where the massive stars and a population of low mass stars are formed in densest, central region of the cluster, while some additional lower mass content would be formed in the outer filamentary structure and then accreted to the cluster centre over its first few Myr, up to the gas expulsion phase. At this point, loss of the gaseous content would greatly reduce the cluster



gravitational potential halting the stars accretion and leading to a rapid expansion. This appears to be confirmed by our older cluster group, with ages greater than 4 Myr, presenting slightly larger stellar densities and steeper MF slopes that are more compatible with the IMF.

A similar scenario have been recently found concerning the star formation in the DR21 ridge (our BDB57 cluster) and its nearby filamentary structure by [Hennemann et al. \(2012\)](#) based on the local gas dynamics and *Herschel* maps. The gravitationally unstable outward filaments forms cores and protostars which flows, along with the gas, towards the the central ridge (the cluster), where most of the densest and more massive cores resides. This behaviour was also observed in the gas content of other star forming regions ([Schneider et al. 2013](#)), but has yet to be observed on the stellar content of a nascent cluster.

## 6.2 Cygnus-X North

By examining our extinction distributions across our clusters, we have found that the extinction towards the Cygnus-X north presents a stable minimum of about 5-6 mag. towards the more evolved clusters in the complex, possibly amounting to the foreground gaseous content. When accounting for this foreground layer, the local extinction in this complex appears to amount to just 1-2 mag. for the evolved clusters (age > 4 Myr) while spanning values between 5-7 mag. in most of the younger ones. Interestingly, even though the older clusters presented slightly sharper extinction distributions, this difference was found to be small across our clusters, as they showed about the same extinction dispersion (evaluated as the FWHM of the distribution) of about 2-3 mag. around their peak value. Since this dispersion generally represents the intra-cluster variation of the extinction column, its somewhat constant value might be tied to similar spatial depths shared by these clusters.

Estimated distances to these clusters appears to confirm previous segregation of the gaseous structure of this region into three layers ([Gottschalk et al. 2012](#)) at distances of ~500-950 pc (LK12, LK14 LK13, BDB57), ~1.4-1.7 kpc (FSR249, BDB59, LK15, BDB56) and >2.5 kpc (BDB58).

The estimated distances to the clusters belonging to the second layer, particularly that of BDB56, the southernmost cluster in our sample (1.4-1.6 kpc), agree very well with recent estimates to Cygnus-OB2 association (e.g 1.4 kpc - [Hanson 2003](#)), pointing out to a possible common origin between the association and southern part of Cygnus-X complex. Given the youth of this cluster (1-4 Myr) and the relatively small distance to the association (~40 pc at 1.4 kpc), a triggered formation scenario is not unlikely considering that Cygnus OB2 could be aged up to 10 Myr.

## 7 CONCLUSION

We have performed an unprecedentedly deep survey of the Cygnus-X north complex in the near-infrared unveiling a rich population of low mass stars and embedded stellar clusters in this region. By developing a tool to properly account for the complex extinction pattern in the region and infer the most probable age and distance of a stellar population, we have been able to uniformly characterise a dozen mostly unstudied clusters throughout this region.

Our results points out that these populations were likely born inside dense, embedded stellar structures of about one parsec size and presenting slightly shallower mass functions slopes than the

IMF, thus presumably lacking some of its lower mass content. Although by themselves the slopes provides evidence against the universality of the IMF, additional cluster parameters (i.e. age, stellar density) appear to support a scenario were these very young clusters are likely to accrete additional low mass stars formed in their vicinity during their first few Myr, reaching the age of 4 Myr with a fully fledged IMF inside their tidal radius. The gas expulsion phase at about 3 Myr would play an important role in halting this process.

Fittings of log-normal mass functions at the low mass domain ( $m < 1 M_{\odot}$ ) points out that the general system IMF in this region appears to have a fairly robust characteristic mass ( $m_c = 0.32 \pm 0.08$ ), that is compatible with those found in other regions, but presents a narrower mass dispersion ( $\sigma_m = 0.40 \pm 0.06$ ) with respect to other young clusters.

Clustered star formation appears to be happening in Cygnus-X north in three different layers, located at distances of 500-950 pc, 1.4-1.7 kpc and 3.0 kpc, consistent with previous distances estimates for The Great Cygnus Rift, the W75N region and the DR21 filament, respectively. Finally, at least one young cluster at the southern part of Cygnus-X north has distance compatible with that of the Cygnus-OB2 association, implying that some interaction may have taken place between these two regions.

## ACKNOWLEDGMENTS

The authors would like to thank the anonymous referee for the suggestions and critics that contributed to greatly enhance this work. The authors acknowledge the support of the brazilian funding agencies CAPES, CNPq. This work was funded in part by the French national research agency through ANR 2010 JCJC 0501-1 "DESC" (PI E. Moraux). Based on observations obtained with WIRCam, a joint project of CFHT, Taiwan, Korea, Canada, France, and the Canada-France-Hawaii Telescope (CFHT) which is operated by the National Research Council (NRC) of Canada, the Institute National des Sciences de l'Univers of the Centre National de la Recherche Scientifique of France, and the University of Hawaii. This research has made use of the NASA/ IPAC Infrared Science Archive, which is operated by the Jet Propulsion Laboratory, California Institute of Technology, under contract with the National Aeronautics and Space Administration. This publication makes use of data products from the Two Micron All Sky Survey, which is a joint project of the University of Massachusetts and the Infrared Processing and Analysis Center/California Institute of Technology, funded by the National Aeronautics and Space Administration and the National Science Foundation. This research has made use of the SIMBAD database and of the Vizier catalogue access tool, operated at CDS, Strasbourg, France

## REFERENCES

- Bastian N., Covey K. R., Meyer M. R., 2010, *ARA&A*, 48, 339
- Beerer I. M., et al., 2010, *ApJ*, 720, 679
- Bertin E., Mellier Y., Radovich M., Missonnier G., Didelon P., Morin B., 2002, *ASPC*, 281, 228
- Bertin E., 2006, *ASPC*, 351, 112
- Bertin E., 2011, *ASPC*, 442, 435
- Bica E., Bonatto C., Dutra C. M., 2003, *A&A*, 405, 991
- Bica E., Dutra C.M., Barbuy B., 2003, *A&A*, 397, 177
- Bonatto C., Bica E., 2007, *MNRAS*, 377, 1301
- Bressan A., Marigo P., Girardi L., Salasnich B., Dal Cero C., Rubele S., Nanni A., 2012, *MNRAS*, 427, 127

- Campbell M. F., Niles D., Nawfel R., Hawrylycz M., Hoffmann W. F., Thronson H. A., Jr., 1982, *ApJ*, 261, 550
- Carroll B. W., Ostlie D. A., 2006, *ima.book*,
- Chabrier G., 2005, *ASSL*, 327, 41
- Cong H. I. L., 1977, *PhDT*,
- Comerón F., Torra J., 2001, *A&A*, 375, 539
- Comerón F., Pasquali A., Figueras F., Torra J., 2008, *A&A*, 486, 453
- Comerón F., Pasquali A., 2012, *A&A*, 543, A101
- Davis C. J., Kumar M. S. N., Sandell G., Froebrich D., Smith M. D., Currie M. J., 2007, *MNRAS*, 374, 29
- Dias W. S., Monteiro H., Caetano T. C., Oliveira A. F., 2012, *A&A*, 539, A125
- Dib S., 2014, *MNRAS*, 444, 1957
- Dutra C. M., Bica E., 2001, *A&A*, 376, 434
- Froebrich D., Scholz A., Raftery C. L., 2007, *MNRAS*, 374, 399
- Froebrich D., Schmeja S., Samuel D., Lucas P. W., 2010, *MNRAS*, 409, 1281
- Gvaramadze V. V., Miroshnichenko A. S., Castro N., Langer N., Zharikov S. V., 2014, *MNRAS*, 437, 2761
- Gottschalk M., Kothes R., Matthews H. E., Landecker T. L., Dent W. R. F., 2012, *A&A*, 541, A79
- Gouliermis D. A., Schmeja S., Dolphin A. E., Gennaro M., Tognelli E., Prada Moroni P. G., 2012, *ApJ*, 748, 64
- Hanson M. M., 2003, *ApJ*, 597, 957
- Hanson M. M., Luhman K. L., Rieke G. H., 2002, *ApJS*, 138, 35
- Hennemann M., et al., 2012, *A&A*, 543, L3
- Hernandez X., Valls-Gabaud D., 2008, *MNRAS*, 383, 1603
- Hodapp K.-W., 1994, *ApJS*, 94, 615
- Humphreys R. M., 1978, *ApJS*, 38, 309
- Hunter T. R., Taylor G. B., Felli M., Tofani G., 1994, *A&A*, 284, 215
- Jørgensen B. R., Lindegren L., 2005, *A&A*, 436, 127
- Kalirai J. S., et al., 2014, *AAS*, 223, #112.05
- Kharchenko, N. V., Piskunov, A. E., Schilbach, E., Röser, S., & Scholz, R.-D. 2013, *A*, 558, A53
- King I., 1962, *AJ*, 67, 471
- Knödseder J., 2000, *A&A*, 360, 539
- Krone-Martins A., Moitinho A., 2014, *A&A*, 561, A57
- Kroupa P., Weidner C., Pflamm-Altenburg J., Thies I., Dabringhausen J., Marks M., Maschberger T., 2013, *pss5.book*, 115
- Kryukova E., et al., 2014, *AJ*, 148, 11
- Kuhn M. A., et al., 2014, *ApJ*, 787, 107
- Le Duigou J.M., Knödseder J., 2002, *A&A*, 392, 869
- Lombardi M., Alves J., Lada C. J., 2006, *A&A*, 454, 781
- Maia F. F. S., Corradi W. J. B., Santos J. F. C., Jr., 2010, *MNRAS*, 407, 1875
- Maia F. F. S., Piatti A. E., Santos J. F. C., 2014, *MNRAS*, 437, 2005
- Majewski S. R., Zasowski G., Nidever D. L., 2011, *ApJ*, 739, 25
- Marston A. P., et al., 2004, *ApJS*, 154, 333
- Miville-Deschênes M.-A., Lagache G., 2005, *ApJS*, 157, 302
- Monteiro H., Dias W. S., Caetano T. C., 2010, *A&A*, 516, A2
- Moraux E., Bouvier J., Stauffer J. R., Barrado y Navascués D., Cuillandre J.-C., 2007, *A&A*, 471, 499
- Moraux E., Bouvier J., Stauffer J. R., Cuillandre J.-C., 2003, *A&A*, 400, 891
- Naylor T., Jeffries R. D., 2006, *MNRAS*, 373, 1251
- Odenwald S. F., Schwartz P. R., 1993, *ApJ*, 405, 706
- Offner S. S. R., Clark P. C., Hennebelle P., Bastian N., Bate M. R., Hopkins P. F., Moraux E., Whitworth A. P., 2014, *prpl.conf*, 53
- Paladini R., Burigana C., Davies R.D., Maino D., Bersanelli M., Cappellini B., Platania P., Smoot G., 2003, *A&A*, 397, 213
- Perren G. I., Vázquez R. A., Piatti A. E., 2015, *A&A*, 576, A6
- Persi P., Tapia M., Smith H. A., 2006, *A&A*, 445, 971
- Pestalozzi M. R., Minier V., Booth R. S., 2005, *A&A*, 432, 737
- Pfalzner S., Kaczmarek T., 2013, *A&A*, 555, A135
- Portegies Zwart S. F., McMillan S. L. W., Gieles M., 2010, *ARA&A*, 48, 431
- Rawlings M. G., Adamson A. J., Whittet D. C. B., 2000, *ApJS*, 131, 531
- Rieke G. H., Lebofsky M. J., 1985, *ApJ*, 288, 618
- Roberts M. S. E., Romani R. W., Kawai N., 2001, *ApJS*, 133, 451
- Rygl K. L. J., et al., 2012, *A&A*, 539, A79
- Sánchez N., Alfaro E. J., 2009, *ApJ*, 696, 2086
- Sarro L. M., et al., 2014, *A&A*, 563, A45
- Scandariato G., Robberto M., Pagano I., Hillenbrand L. A., 2011, *A&A*, 533, A38
- Schneider N., Bontemps S., Simon R., Jakob H., Motte F., Miller M., Kramer C., Stutzki J., 2006, *A&A*, 458, 855
- Schneider N., et al., 2013, *A&A*, 551, C1
- Shepherd D. S., Kurtz S. E., Testi L., 2004, *ApJ*, 601, 952
- Siess L., Dufour E., Forestini M., 2000, *A&A*, 358, 593
- Skrutskie M. F., et al., 2006, *AJ*, 131, 1163
- Torrelles J. M., Gómez J. F., Rodríguez L. F., Ho P. T. P., Curiel S., Vázquez R., 1997, *ApJ*, 489, 744
- Treyer M., Wyder T., Neill J., Seibert M., Lee J., 2011, *ASPC*, 440,
- Wright N. J., Drew J. E., Mohr-Smith M., 2015, *MNRAS*, 449, 741

## APPENDIX A: ANALYSIS CHARTS

All the plots and figures generated in the analysis of our clusters were compiled into full page charts, presented in Figs. [A1-A10](#), through this appendix.

This paper has been typeset from a  $\text{\LaTeX}$  file prepared by the author.



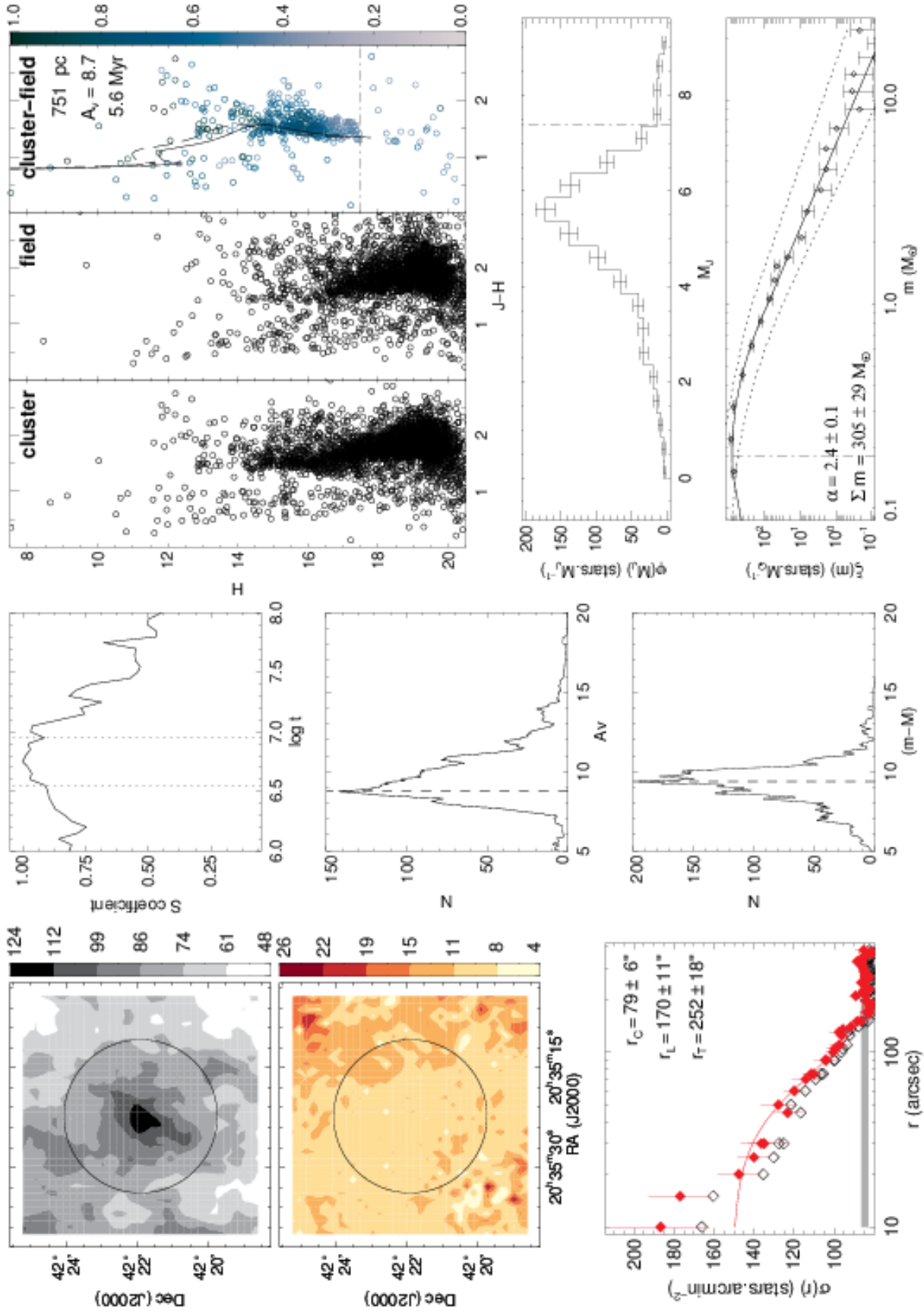


**Figure A1.** LK12 analysis charts. Top-left: general density map showing the cluster extraction radius (solid line). Centre-left: extinction map of the cluster vicinity. Bottom-left: RDP showing the derived structural parameters. Top-middle: S coefficient (solid line) showing the adopted age interval (vertical dotted lines). Bottom-middle: extinction and distance modulus distribution from which their expected values (vertical dashed lines) were derived. Top-right: CMDs comparing the cluster, field and decontaminated samples; single-star (solid line) and same mass binary (dashed line) isochrones with the most probable physical parameters are shown. Bottom-right: derived LF showing the MF fitting limit (vertical dot-dashed line) and derived mass distribution showing the best MF fit (solid line) and the expected IMF domain (dotted lines).

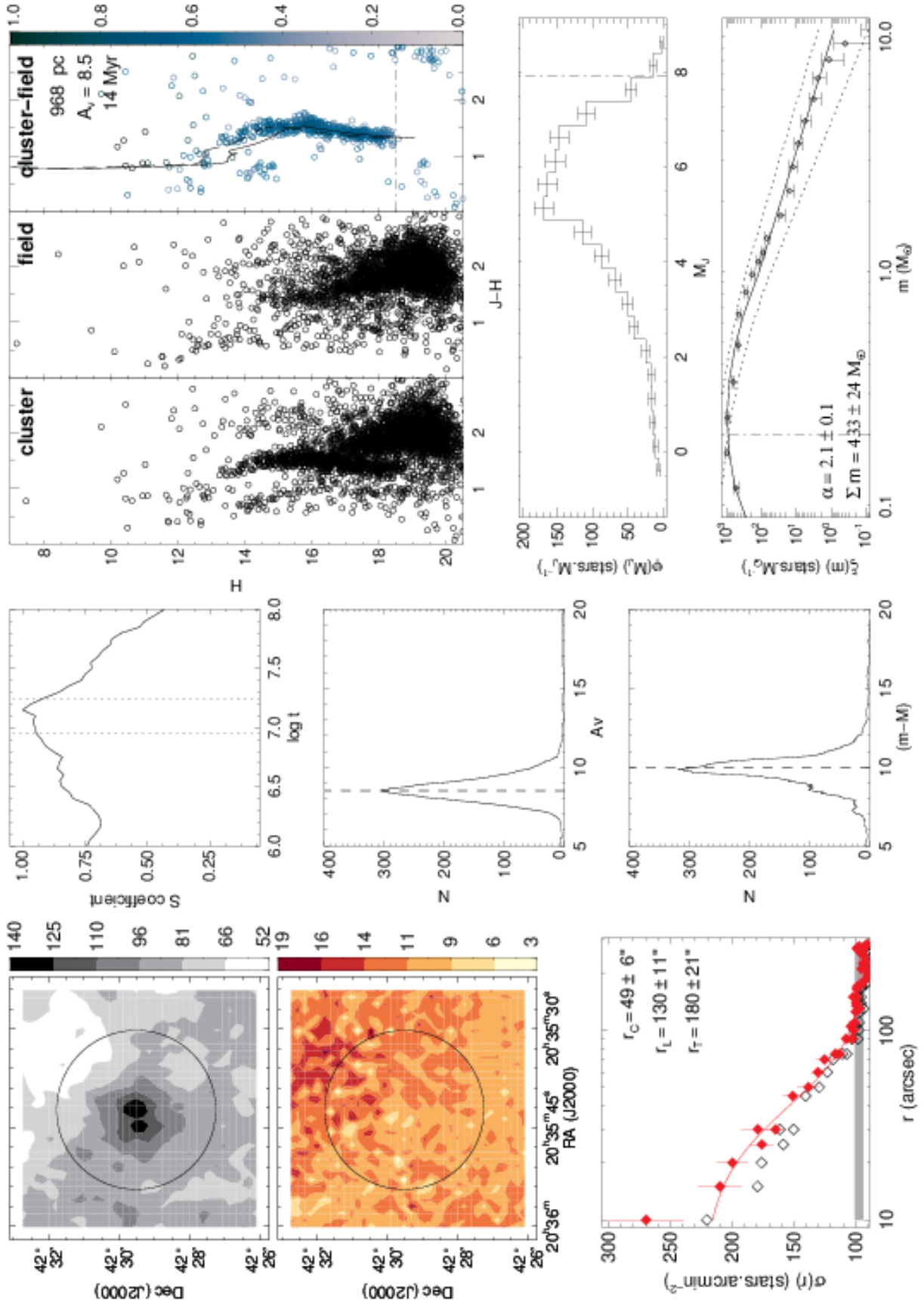


Figure A2. LK14 analysis charts. Panels are the same as in Fig. A1.

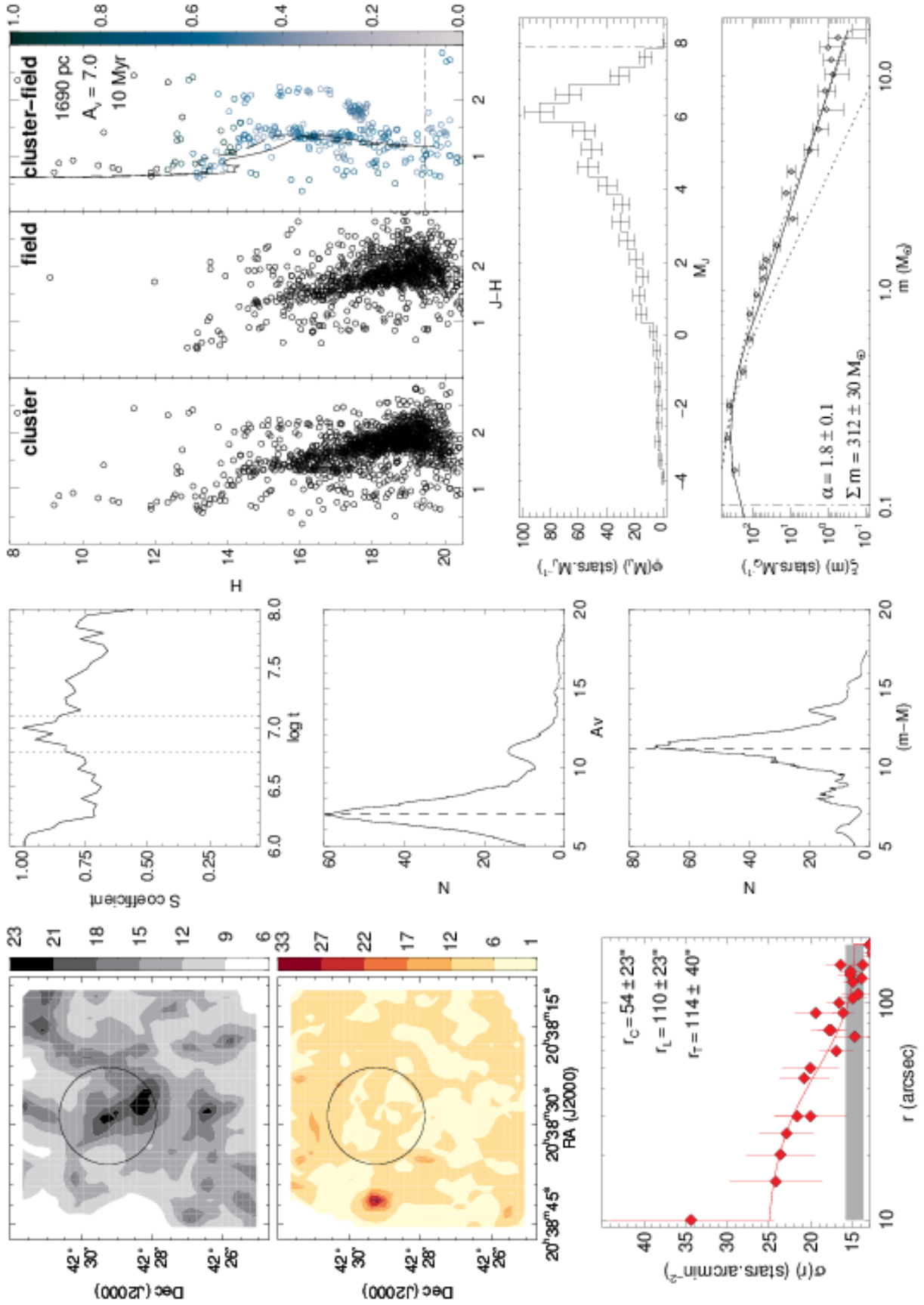


Figure A3. FSR249 analysis charts. Panels are the same as in Fig. A1.

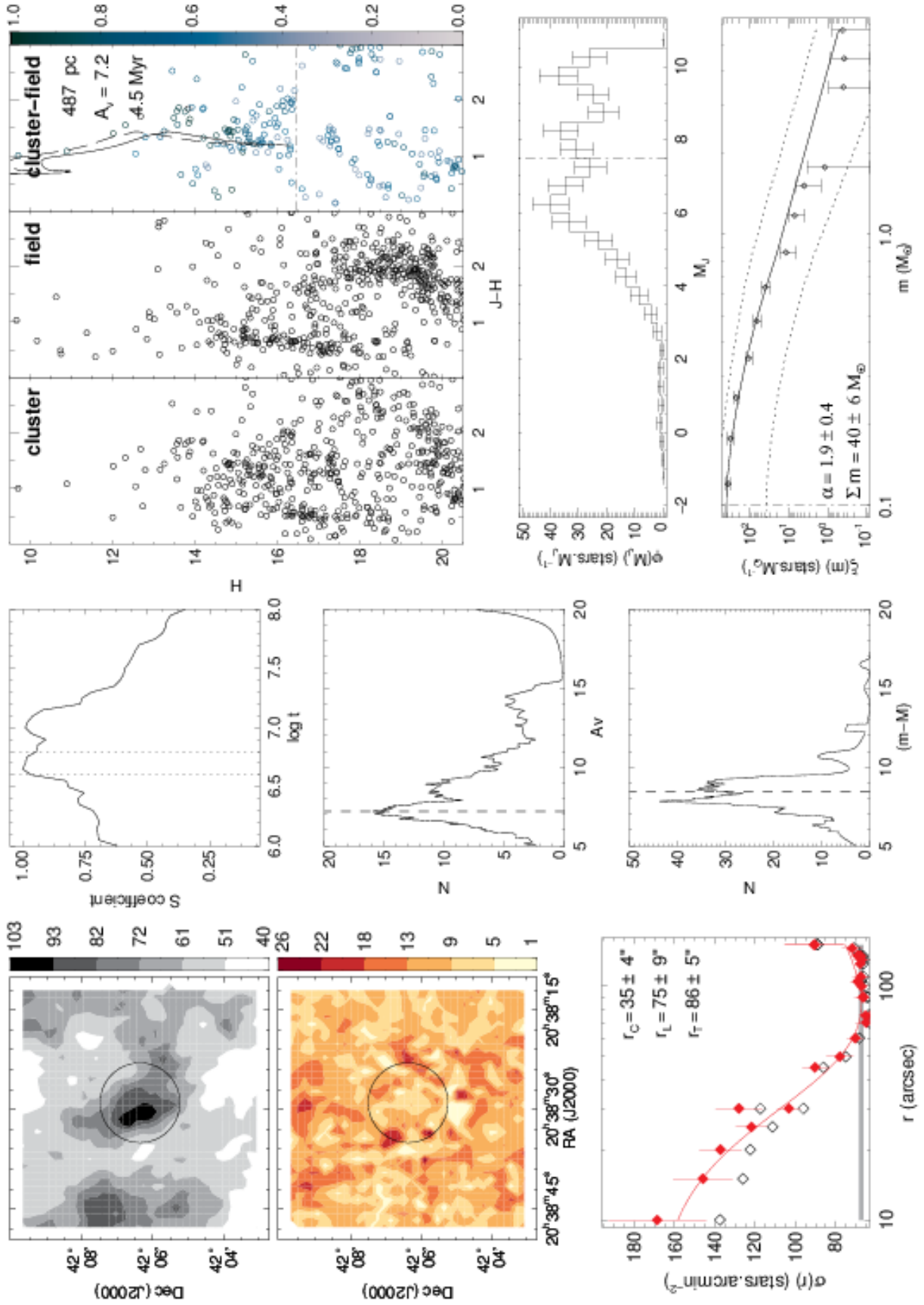


Figure A4. LK13 analysis charts. Panels are the same as in Fig. A1.



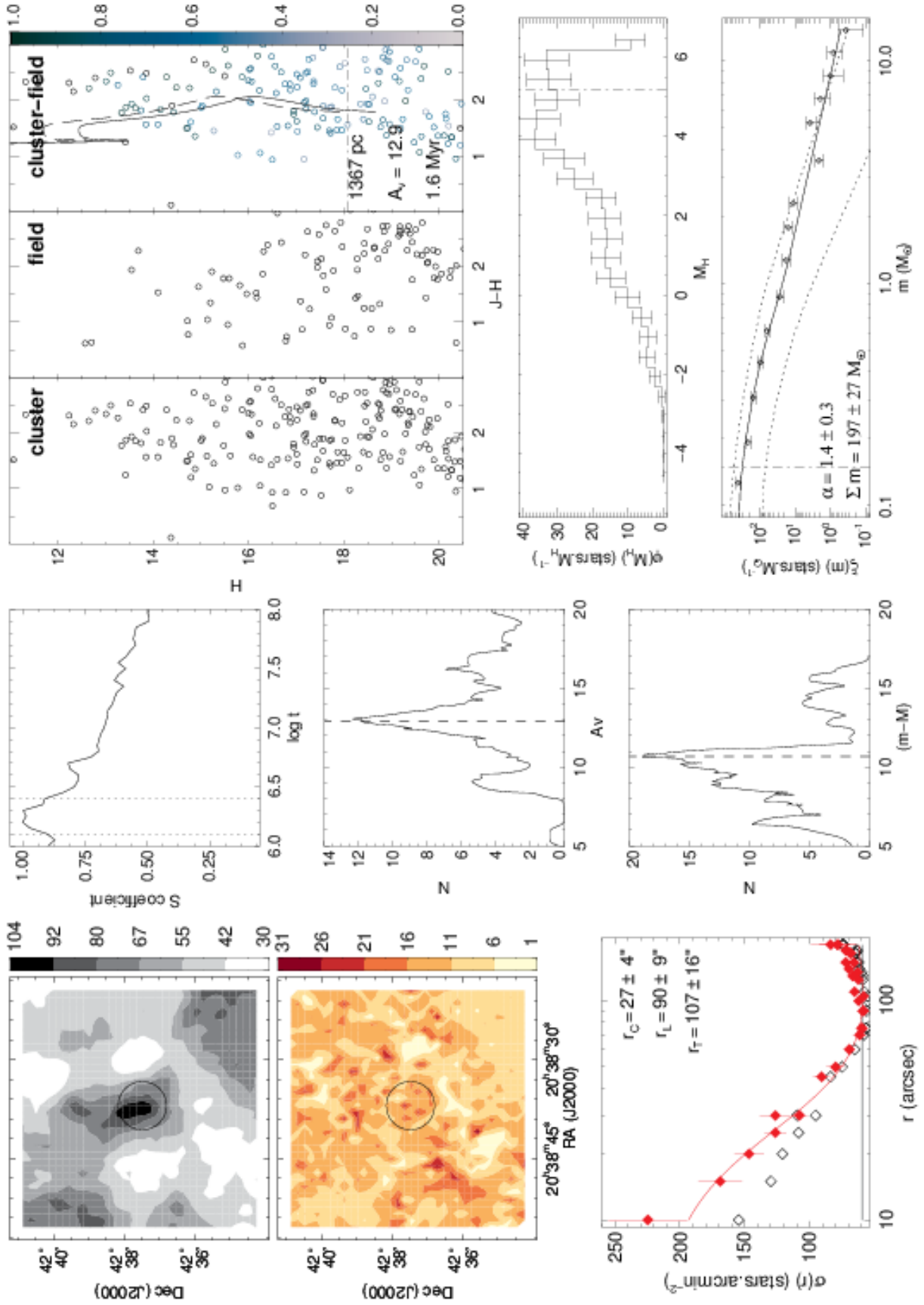


Figure A5. BDB59 analysis charts. Panels are the same as in Fig. A1.

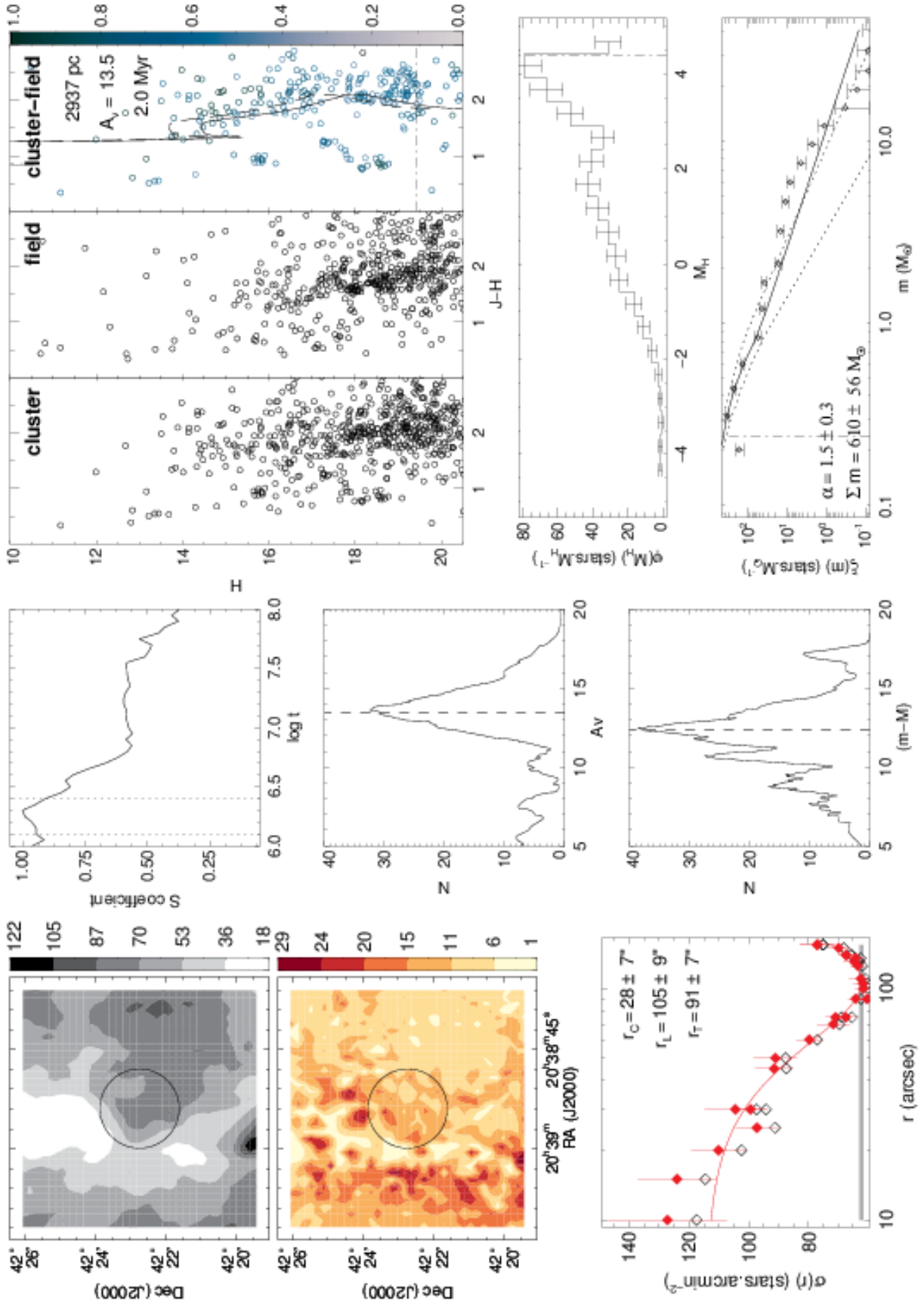


Figure A6. BDB58 analysis charts. Panels are the same as in Fig. A1.

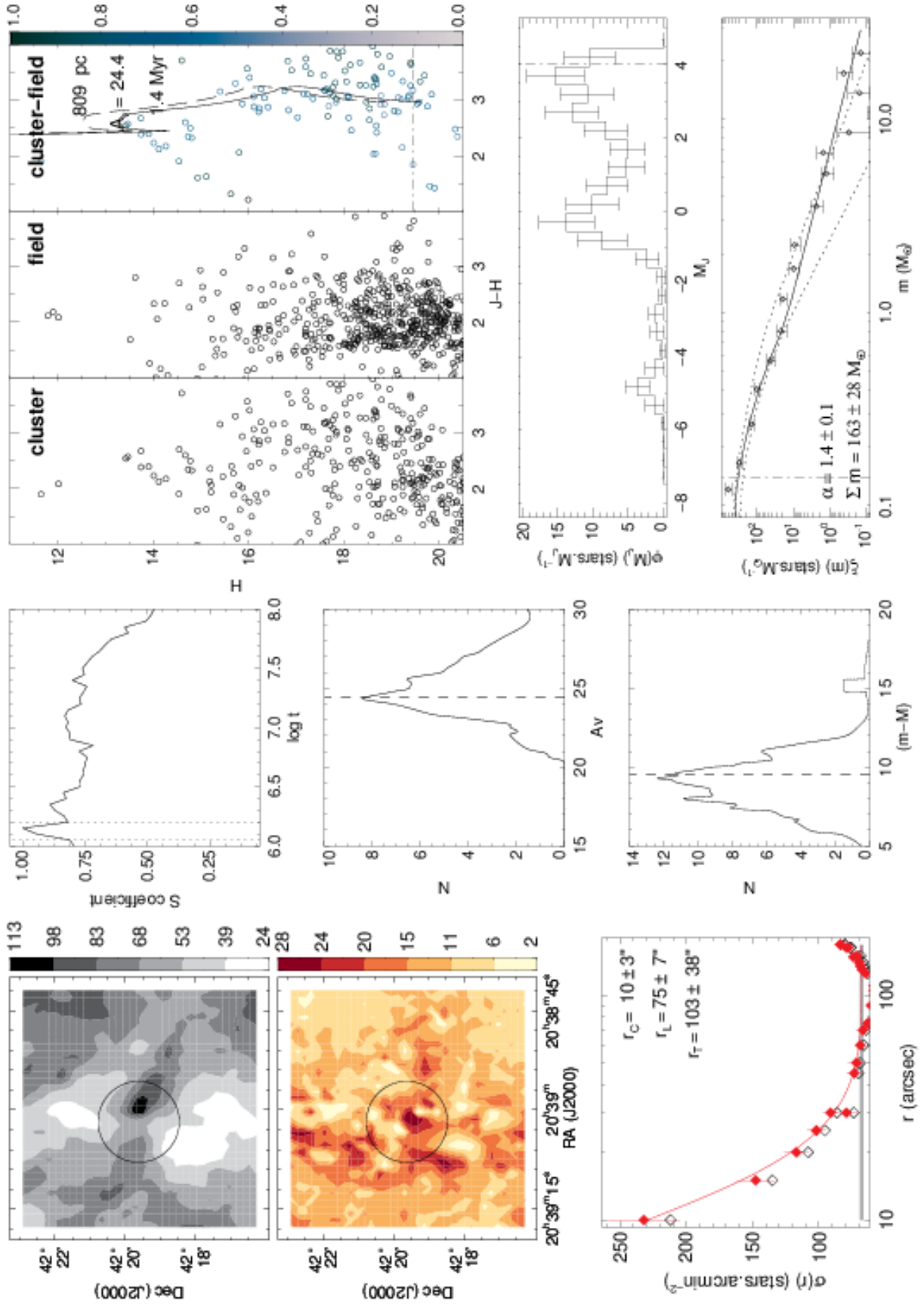


Figure A7. BDB57 analysis charts. Panels are the same as in Fig. A1.

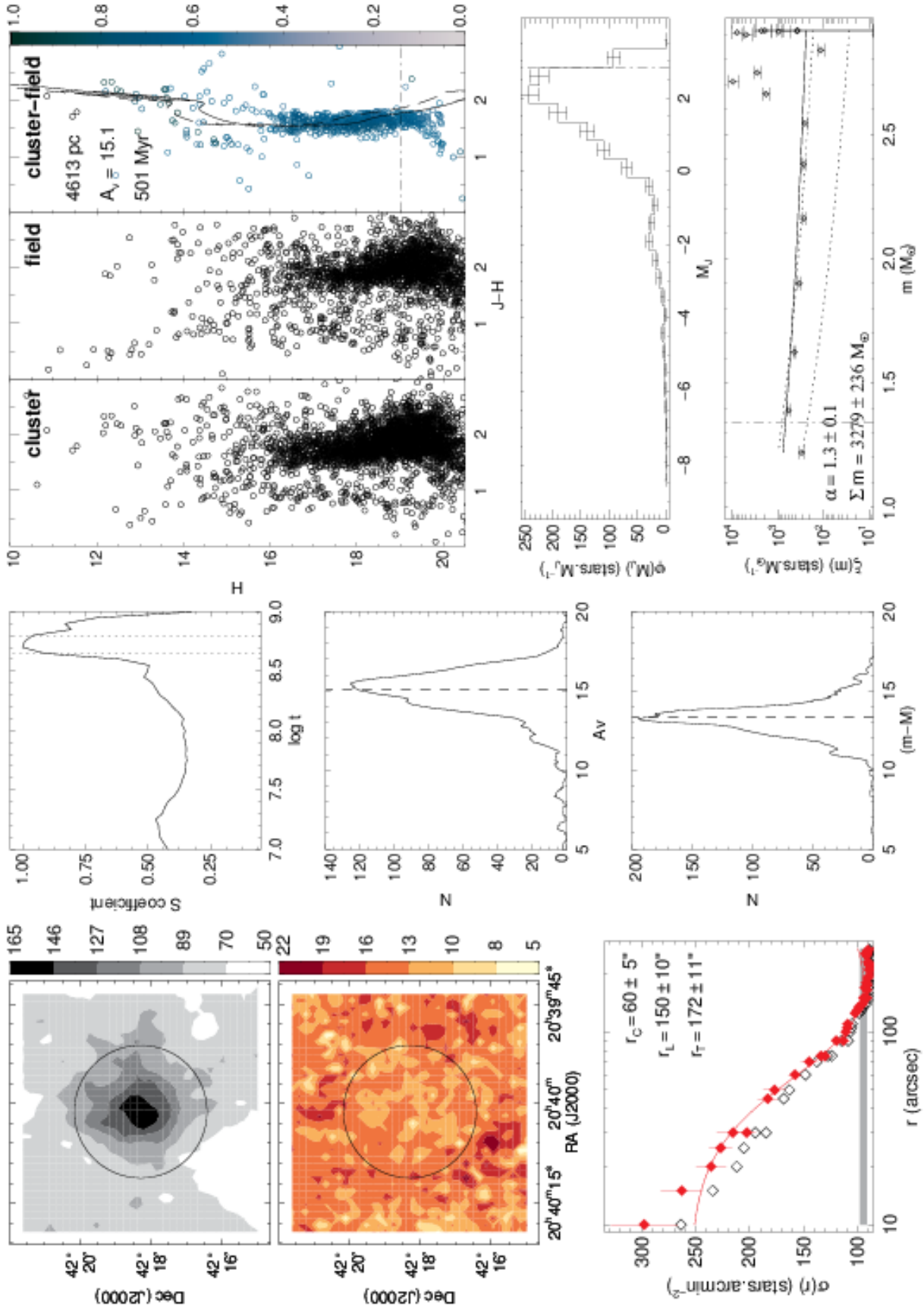


Figure A8. Bica3 analysis charts. Panels are the same as in Fig. A1.



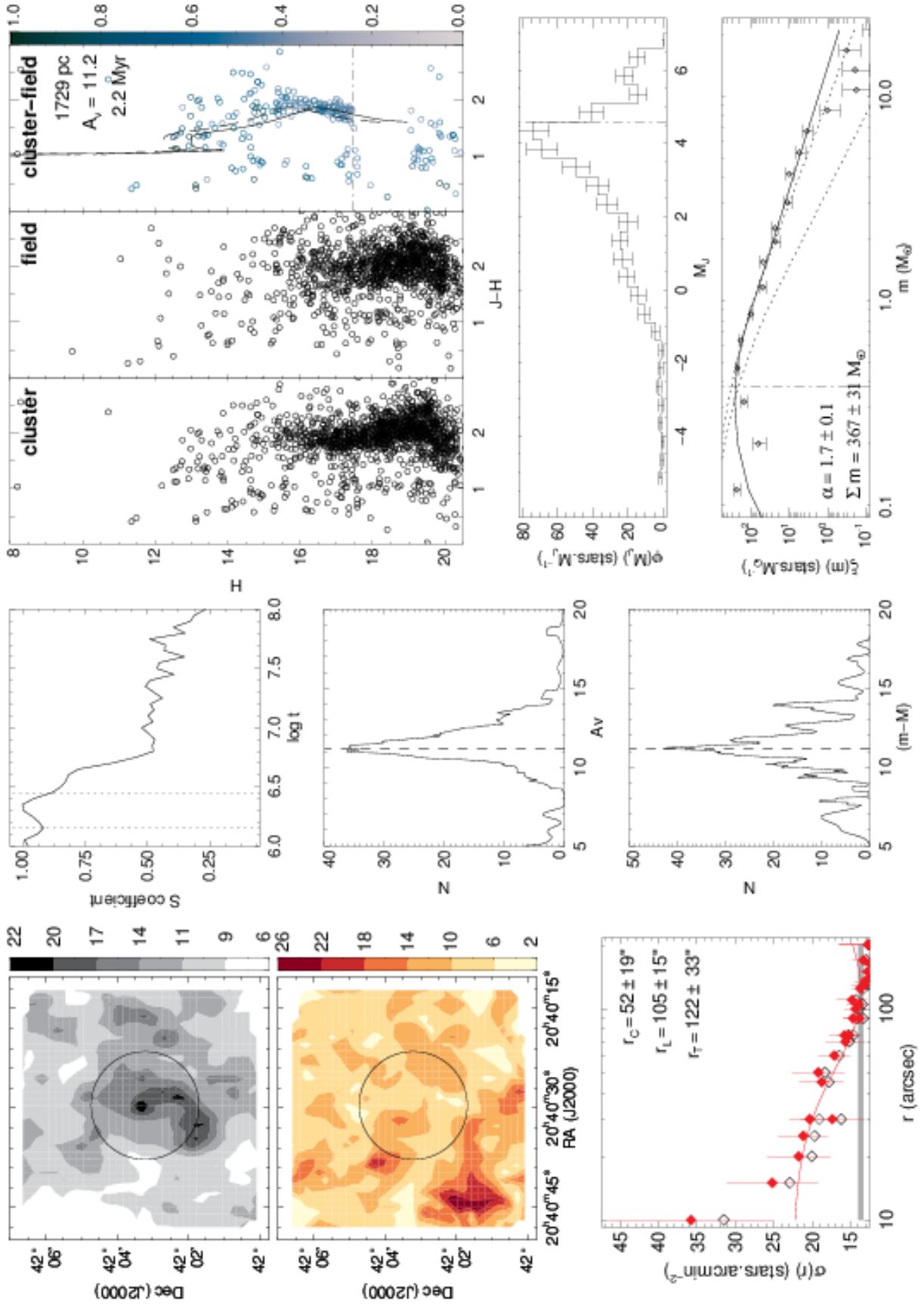


Figure A9. LK15 analysis charts. Panels are the same as in Fig. A1.

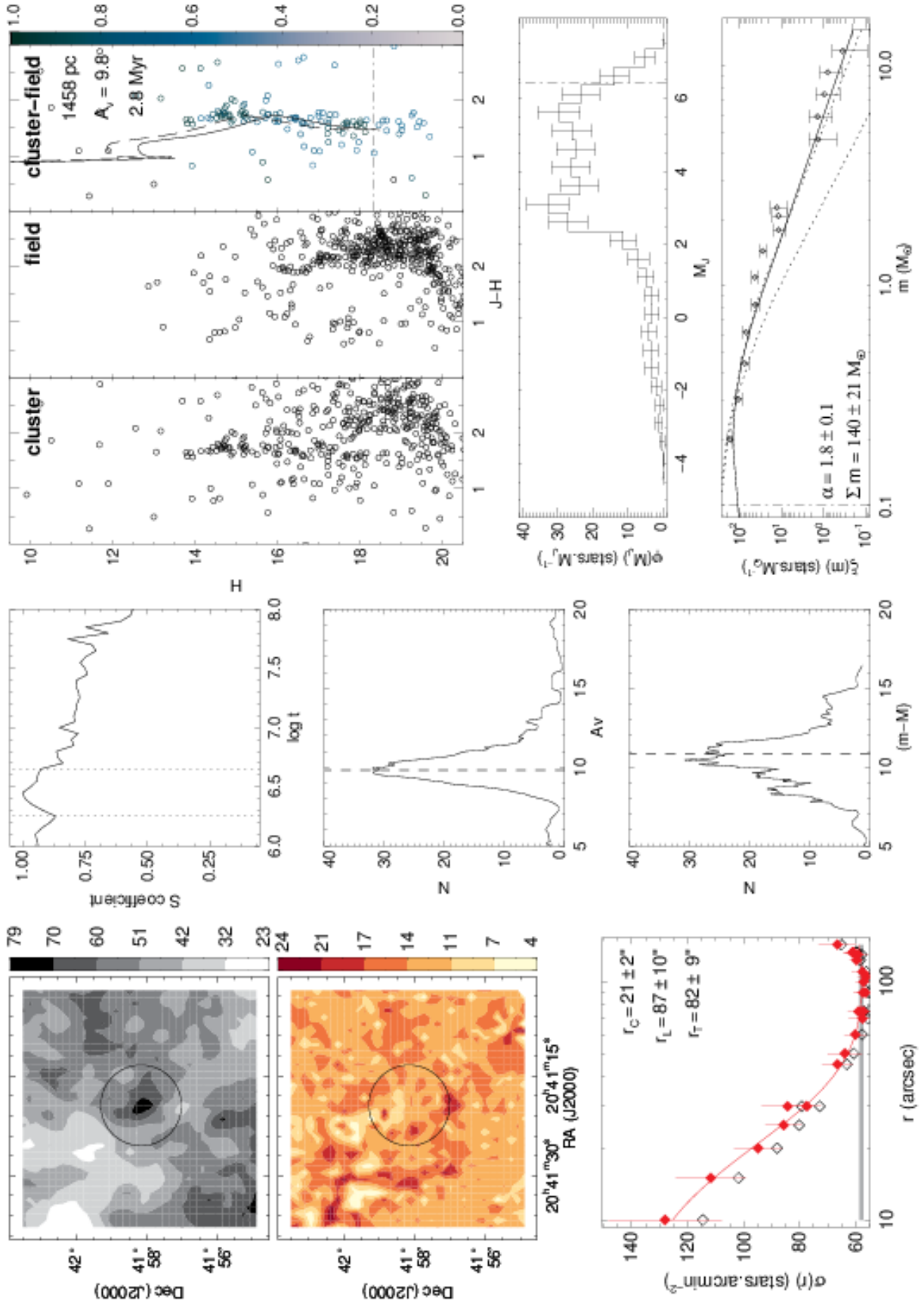


Figure A10. BDB56 analysis charts. Panels are the same as in Fig. A1.